Ferroelectricity and Antiferroelectricity of Doped Thin HfO2-Based Films

Min Hyuk Park, Young Hwan Lee, Han Joon Kim, Yu Jin Kim, Taehwan Moon, Keum Do Kim, Johannes Müller, Alfred Kersch, Uwe Schroeder, Thomas Mikolajick, and Cheol Seong Hwang*

The recent progress in ferroelectricity and antiferroelectricity in HfO2-based thin films is reported. Most ferroelectric thin film research focuses on perovskite structure materials, such as Pb(Zr,Ti)O3, BaTiO3, and SrBi2Ta2O9, which are considered to be feasible candidate materials for non-volatile semiconductor memory devices. However, these conventional ferroelectrics suffer from various problems including poor Si-compatibility, environmental issues related to Pb, large physical thickness, low resistance to hydrogen, and small bandgap. In 2011, ferroelectricity in Si-doped HfO2 thin films was first reported. Various dopants, such as Si, Zr, Al, Y, Gd, Sr, and La can induce ferroelectricity or antiferroelectricity in thin HfO2 films. They have large remanent polarization of up to 45 μC cm^{-2}, and their coercive field (≈1–2 MV cm^{-1}) is larger than conventional ferroelectric films by approximately one order of magnitude. Furthermore, they can be extremely thin (<10 nm) and have a large bandgap (>5 eV). These differences are believed to overcome the barriers of conventional ferroelectrics in memory applications, including ferroelectric field-effect-transistors and three-dimensional capacitors. Moreover, the coupling of electric and thermal properties of the antiferroelectric thin films is expected to be useful for various applications, including energy harvesting/storage, solid-state-cooling, and infrared sensors.

1. Introduction

Ferroelectricity was first reported in Rochelle salt by Valasek in the early 1920s, and it has been studied intensively for various applications including microelectromechanical systems (MEMS), radio-frequency identification (RFID) chips, and semiconductor memory devices.[1–4] Ferroelectric (FE) materials have two remanent polarization states $\pm P_r$ even after the electric bias is removed, and these two P_r states can be "0" and "1" states for memory applications.[3,4] FE materials have many other promising properties, such as pyroelectricity, piezoelectricity, and a high dielectric constant ε_r, which have already been utilized in commercial uses for various electronic, optical devices, and sensors.[3] Recently, their electro-thermal performances, i.e., their electrocaloric effect (ECE), make them an important material for energy-related applications.[5–8] All the details for such a vast range of functionalities cannot be discussed in a single report, and this report limits its main concern to the application of FE materials for electrical memory applications and the possible electro-thermal effects of recently found FE HfO2-based thin films.

Most of the electronic devices utilizing FE thin films, such as the ferroelectic random access memory (FeRAM), have been based on perovskite structured materials, like Pb(Zr,Ti)O3 (PZT), BaTiO3 (BTO), and SrBi2Ta2O9 (SBT), which are classified as "conventional" FE thin films in this report.[4] Although some of the conventional ferroelectrics such as BaTiO3 can be epitaxially grown on a Si substrate by carefully optimizing the fabrication process,[9] the quality of the interface between the FE layer and the Si substrate is inappropriate in most cases.[10] Generally, an interfacial SiO2 layer is formed and the resulting depolarization field weakens the stability of the bistable polarization states. Therefore, the direct integration of the conventional FE thin films on Si substrates has not been successful. As a consequence, the metal/FE/metal capacitors have been used in FeRAM, and metal electrodes are connected to the drain region of a Si transistor through a metallic contact.[11] In an FE field-effect-transistor (FeFET), where the FE layer is integrated into the gate stack of the field-effect transistor (FET), the

Dr. M. H. Park, Y. H. Lee, H. J. Kim, Y. J. Kim,
T. Moon, K. D. Kim, Prof. C. S. Hwang
Department of Materials Science and Engineering
Seoul National University
Seoul 151–744, Republic of Korea
E-mail: cheolsh@snu.ac.kr
Dr. M. H. Park, Y. H. Lee, H. J. Kim, Y. J. Kim,
T. Moon, K. D. Kim, Prof. C. S. Hwang
Inter-university Semiconductor Research Center
College of Engineering
Seoul National University
Seoul 151–744, Republic of Korea
Dr. J. Müller
Fraunhofer IPMS-CNT
Koenigsbruecker Str. 178, 01109 Dresden, Germany
Prof. A. Kersch
University of Applied Sciences Munich
Lothstr. 34, 80335 Munich, Germany
Dr. U. Schroeder, Prof. T. Mikolajick
NaMLab gGmbH/TU Dresden
Noethnitzer Str. 64, 01187 Dresden, Germany

quality control of interfacial properties with the channel region of the underlying Si is also extremely challenging.[10] In general, the conventional FE materials have several inherent weaknesses related to their relatively small electrical bandgap (E_g, 3–4 eV), which induces a Schottky barrier height of only ≈1 eV with respect to the metal electrodes.[4] This makes them vulnerable to leakage current and electrical breakdown.[4] Therefore, a relatively large film thickness (t_f ≈100 nm) is required for the capacitive layer of charge-based FeRAM, which has hindered the facile fabrication of three-dimensional capacitor structures for the technology node with a thicknesses of a few tens of nanometers.[12] The relatively weak bonding energy of oxygen with the constituent metal ions in these materials invokes defect-related (mostly oxygen vacancies V_O) reliability concerns, such as fatigue, and imprint and retention failure.[4,13] In addition, the use of Pb-containing materials, including PZT, is prevented in many countries due to environmental issues, despite its outstanding FE performances.[13] Therefore, developing new lead-free FE materials which are compatible with Si with a large E_g, P_r and high bonding energy between the metal ions and oxygen is an urgent task for the future development of FE memories and other related devices. For material scientists, HfO_2 based FEs are of special interest because they are simple binary oxides, and exhibit a non-perovskite structure together with a remarkably low relative permittivity (≈20–30, compared to PZT with 300 or higher). The comparably simple chemistry of the system makes it less prone to perturbing effects during deposition, and eases the theoretical studies by, e.g., ab-initio simulations. Thus, HfO_2 and the chemically comparable ZrO_2 could serve as a model system for a new class of FEs. The origin of an emergence of FE properties in conventional materials has been well explained by the phenomenological approach (Landau–Ginzburg–Devonshire (LGD) theory[14–16], where the total internal energy could have two minima at the states with ±P_r. However, it is still not very clear if the same LGD theory can be directly applied to HfO_2-based FE materials.

There is another type of polarization-ordered state, which is stable under certain bias conditions, whereby the alignment of the polarization vector inside the material becomes anti-parallel under zero-bias condition. Materials having these properties are named antiferroelectric (AFE) materials. The phenomenological theory for antiferroelectricity was first proposed by Kittel in the early 1950s.[17] Different from FE materials, AFE materials are inappropriate for memory applications due to the absence of a macroscopic remanent bistable polarization at zero-bias. Nevertheless, the AFE materials generally show characteristic double hysteresis loops in their polarization–electric field curves, resulting from the field-induced reversible transitions between the FE and AFE phases.[17] AFE materials can be used for various applications such as energy storage,[18–21] pyroelectric energy harvesting (PEH),[18,22] solid state cooling based on the ECE,[17,20,22] and infrared sensing for thermal imaging.[8,24] Another application would be phase change materials, in the sense of mechanical deformation, which would be an important alternative to piezoelectric materials. For these applications, AFE materials with large transition electric fields, large breakdown fields, and large pyroelectric constants are preferred. The Zr-rich PZT-based inorganic materials and Poly(vinylidene fluoride) (PVDF) based polymers have been the
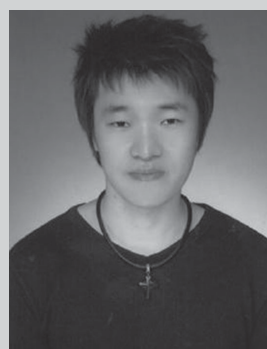
Min Hyuk Park received his B.S. and Ph.D degrees in Materials Science and Engineering from Seoul National University, Seoul, Korea, in 2008 and 2014, respectively. He is currently a postdoctoral researcher in the department of Materials Science and Engineering Seoul National University since March of 2014. His research interests include ferroelectric and antiferroelectric thin films for memory, energy storage, energy harvesting, solid-state cooling, and sensor applications.

Uwe Schroeder received his doctoral degree at University of Bonn, Germany including a research visit at UC Berkeley and worked at University of Chicago as a post-doctoral researcher. He joined Infineon formerly Siemens Semiconductor in 1997 for capacitor development in the DRAM Development Alliance with IBM, before transferring to Infineon's Memory Development Center in Dresden, Germany in 2000. There, he continued the research on high-k dielectrics and their integration into DRAM capacitors. During this time the ferroelectric properties of HfO_2 based dielectrics were found. In 2009 he moved to NaMLab and pursued his work on high-k dielectrics and ferroelectric HfO_2-layers.

Cheol Seong Hwang received his PhD degree from Seoul National University, Seoul, Korea, in 1993. Then, he joined the National Institutes of Standards and Technology, Gaithersburg, MD, as a Postdoctoral Research Fellow. In 1994, he joined the Samsung Electronics Company, Ltd., as a Senior Researcher. Since 1998, he has been a Professor at the Department of Materials Science and Engineering, Seoul National University. His current research interests include high-k gate oxides, dynamic random access memory capacitors, new memory devices including resistive RAM devices and ferroelectric materials and devices, and energy storage capacitors.
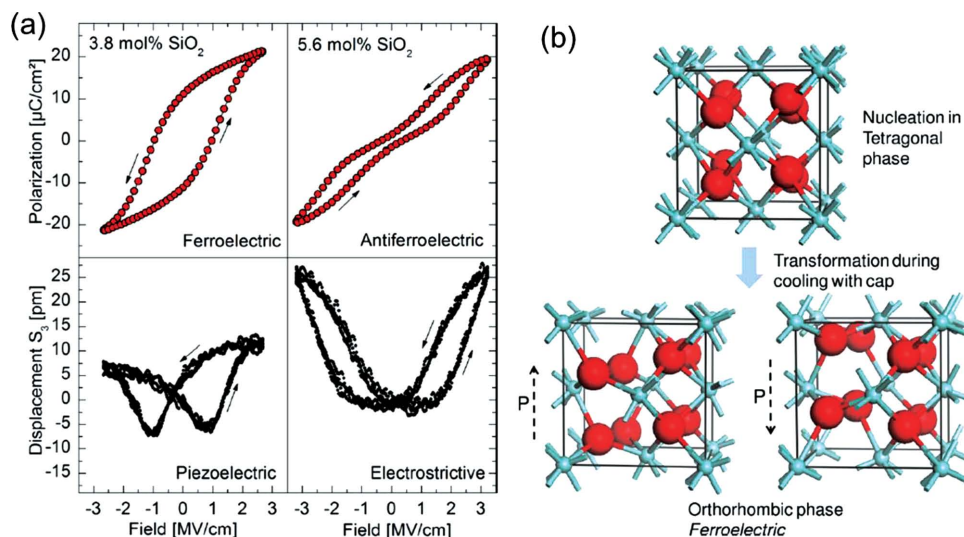
Figure 1. a) Polarization (top row) and piezoelectric displacement (bottom row) measurement of TiN/Si:HfO$_2$/TiN capacitor sample with ferroelectric (left column) and antiferroelectric (right column) composition. b) The formation of the orthorhombic III phase proceeds by transformation from the tetragonal phase during cooling with TiN capping layer. The bottom row indicates two different polarization states of the ferroelectric phase. Reproduced with permission.[29] Copyright 2011, AIP Publishing LLC.

most promising candidates.[5–8,22–24] However, the use of PZT films is limited due to environmental concerns, as aforementioned, and PVDF-based polymers are generally unstable at high temperatures due to their low melting point ($\approx$170 °C).[6,23] Therefore, developing new lead-free AFE materials with a large transition field, a large breakdown field, and robust thermal stability is required.

HfO$_2$ is an electrical insulator with an energy gap of $\approx$5.3–5.7 eV, and its relative dielectric constant ε_r is $\approx$17 in its monoclinic structure, which is the most stable form under usual conditions.[25] The material crystallizes in the monoclinic phase with a space group of P2$_1$/c. It is chemically inert, and has an elastic modulus of larger than 200 GPa.[26] Due to the previously mentioned properties, HfO$_2$ is used as an optical coating and a high-k material in semiconductor industries.[27,28] The ferroelectricity and antiferroelectricity in thin HfO$_2$-based films was first discovered in 2007 by Böscke et al. at dynamic random access memory (DRAM) manufacturer Qimonda when the company was searching for an optimized dielectric material for DRAM capacitors, and verified by the Waser group in Aachen. The experiments continued at NaMLab and Fraunhofer CNT and the result was first published in 2011.[29] **Figure 1**a shows the polarization–electric field (P–E, top row) and piezoelectric displacement–electric field curves (bottom row) of FE (left column) and AFE (right column) 10nm-thick Si-doped HfO$_2$ films.[29] The Si-doped HfO$_2$ films with doping concentration of 3.1–4.3% showed feasible ferroelectricity with remanent polarization P$_r$ of $>\approx$10 μC cm^{-2}. On the other hand, when the Si doping concentration was $>$4.3%, AFE behavior started to emerge, and at sufficiently high Si concentrations ($>$8.5%) the material became a linear dielectric layer with an ε_r of 10–15.[30] In this report, all the doping concentrations represent the cation concentration ([dopant]/{[Hf]+[dopant]}). Since undoped and several impurity-containing HfO$_2$ films have been regarded as typical high-k dielectric materials without any hysteretic behavior, these findings were quite striking. While

further detailed studies are necessary to precisely understand the origin of such unexpected FE and AFE behavior of the HfO$_2$-based films, the beginning part of this report rather focuses on the past knowledge on this behavior. The FE properties of doped HfO$_2$ films have been reported for various dopants, such as Si,[29–35] Zr,[36–42] Y,[43–45] Al,[46,47] Gd,[48] Sr,[49] and La.[50] The various experimental works on the FE and AFE properties of Hf$_{1-x}$Zr$_x$O$_2$ films were also reported by the NaMLab/Fraunhofer CNT collaboration,[37] which were succeeded by the group in Seoul National University, who has focused on the evaluation of the FE and AFE performances and their possible origins for the past three years.[38–42,51–54] The FE and AFE properties of the HfO$_2$-based films with various dopants will be discussed in detail in Section 3. The P$_r$ values of the HfO$_2$-based films are generally in the range of 15–25 μC cm^{-2} for Si-, Al-, Gd-, and Sr-doped films, and Hf$_{1-x}$Zr$_x$O$_2$ films, which is relatively lower than that of PZT. However, a maximum value of $\approx$40 μC cm^{-2} was recently reported from the La-doped HfO$_2$ films, which is quite comparable to the state-of-the-art PZT films with polycrystalline structure.[55–58] Surprisingly, however, the large P$_r$ values of the HfO$_2$-based films could be achieved from $\approx$10 nm t$_f$,[29–50] whereas the t$_f$ of PZT films should be 10^2–10^4 nm to realize its full capability.[59] The small t$_f$ of $\approx$10 nm is a crucial merit for the three-dimensional capacitor fabrication on nanostructure templates, which is highly required for memory and energy storage applications. Even with such a small t$_f$, the possible problems related to the leakage current and reliability issues could be highly mitigated, thanks to the far higher E$_g$ values ($\approx$5.5 eV) and much stronger bonding between oxygen and Hf (with Zr and other dopants) of FE doped HfO$_2$-based films.[29,38,60] The highly matured deposition techniques, such as atomic layer deposition (ALD), which are already employed in mass-production for the high performance transistors, make the films even more promising FE and AFE materials for important applications.[60] Both HfO$_2$ and TiN, which is the most commonly used electrode with FE doped HfO$_2$-based

films, are standard materials for the semiconductor industry.[60] Due to the impressive material performance and matured deposition process, research on FE or AFE HfO$_2$ films is increasing rapidly, and almost 45 papers have been published during the last three years, which inspired the authors to write a progress report on this field.

2. Origin of Ferroelectricity and Antiferroelectricity in Doped HfO$_2$-Based Thin Films

2.1. Computational Investigations

HfO$_2$ (and ZrO$_2$ too) has various polymorphs in the bulk phase depending on the temperature and pressure; the transition from monoclinic (m-phase, number 14, space group P2$_1$/c) to tetragonal (t-phase, number 137, space group P4$_2$/nmc) and to cubic phase (c-phase, number 225, space group Fm3m) occurring at 1973, and 2773 K, respectively, under the atmospheric pressure is most well known,[61] whereas the transitions to various orthorhombic phases with increasing pressure have been less acknowledged. With the increasing hydrostatic compressive pressure, the most stable m-phase transforms into the orthorhombic I phase (oI-phase, at 4 GPa, number 61, space group Pbca) and the orthorhombic II phase (oII-phase, at 14.5 GPa, number 62, space group Pnma).[61] All of the polymorphs of HfO$_2$ in the bulk phase diagram, depending on the temperature and pressure, have inversion symmetry and thus cannot be FE or AFE. However, there exist several further orthorhombic and polar phases, especially the orthorhombic III phase (oIII-phase, number 29, space group Pca2$_1$),[64,65] which is stable under different stress, chemical or surface conditions, and this has been discussed experimentally[65–67] and theoretically.[21,62–64] Recently, Huan et al. systematically examined the polymorphism of HfO$_2$ using the first principle calculation of free energy, including stress and phonon contributions at various temperatures.[62] In their report, a total of 11 stable or metastable polymorphs were found, and two of them were polar. The space groups of these two orthorhombic phases were Pca2$_1$ (the aforementioned oIII-phase) and Pmn2$_1$ (oIV-phase, number 31), and their free energy values were extremely close to those of the equilibrium nonpolar phases under various temperature and pressure ranges.[62] The difference was smaller than k$_B$T/5, where k$_B$ is the Boltzmann constant.[62] Huan et al. also simulated the X-ray diffraction patterns of these two polar phases, and the diffraction pattern of the former (oIII-phase) is believed to be well-matched with those reported in recent works.[62]

Lowther et al. calculated the total energy of various polymorphs of HfO$_2$ and ZrO$_2$ as a function of volume of a unit cell, without including the stress and phonon contributions.[63] They found that the energies of the orthorhombic phases are very similar, and in the case of ZrO$_2$ energies were even less than that of the m-phase.[63] They concluded that the polar oIII-phase could probably be stabilized under a certain range of hydrostatic compressive pressure, or temperature.[63]

The polar oIII-phase was experimentally observed under these conditions in Mg-doped ZrO$_2$ by Kisi.[65] Even though the report was not about the observation of polar phase of

HfO$_2$, it should be noted that ZrO$_2$ is a "twin oxide" of HfO$_2$. In their experiments, the lenticular-shaped t-phase grains were embedded in the c-phase matrix of the Mg-doped ZrO$_2$. A large tensile stress was induced along the c-axis, and a small compressive stress was developed along the a- and b-axis directions of the t-phase, due to the difference in the anisotropic coefficient of thermal expansion (CTE) of the two phases upon cooling from room temperature (RT) to 80 K. The CTE of the c-axis of the t-phase (1.43 × 10^{-5} °C^{-1}) was larger than that of the c-phase (1.11 × 10^{-5} °C^{-1}), whereas those of the a- and b-axis (1.01 × 10^{-5} °C^{-1}) were smaller than that of the c-phase.[65] The magnitude of the tensile stress on the c-axis needed for the phase transition was calculated to be ≈3.6 GPa.[65] Kisi reported that the space group of the polar oIII-phase was Pbc2$_1$,[65] which is, in fact, identical to that of the Pca2$_1$ oIII-phase in the aforementioned theoretical calculation. (In fact, Pbc2$_1$ is not a standard notation for the space group; it is conjectured that he misused the notation.) The oIII-phase can have P$_r$ along its polar c-axis, although its value had not been reported experimentally before the pioneering report by Böscke et al.[29] From the density functional calculations, the first computed value of P$_r$ was published by Clima et al. with approximate values of 40–53 μC cm^{-2} for HfO$_2$ doped with various dopants, which will be discussed in detail in Section 3.[68] Reyes-Lillo et al. and Huan et al. also conducted computational calculations and reported a P$_r$ of ≈58 and ≈52 μC cm^{-2} for the oIII-phase HfO$_2$.[21,62] The experimental P$_r$ values (12–24 μC cm^{-2}, except the La-doped HfO$_2$) are 30–45% of the theoretical values.[29–49] It should be noted that the c-axis of the oIII-phase is not the crystallographic direction with the largest lattice parameter. Therefore, when a large tensile stress was applied along the c-axis of the t-phase, the direction normal to the c-axis of the t-phase could be the polar direction of the oIII-phase after the phase transition.[40]

Possible origins of the antiferroelectricity in ZrO$_2$ and HfO$_2$ were first examined by Reyes-Lillo et al. using density functional calculations.[21] As predicted by Böscke et al.,[29] they found that there could be first-order transitions between the nonpolar t-phase and the polar oIII-phase with a very low activation energy of 35meV per formula unit (3.4 kJ mol^{-1}), and constructed a Landau–Devonshire model for the phase transition.[21] This suggests that the AFE behavior experimentally observed in thin films could be an intrinsic crystalline property and not a pinning–depinning of the FE domains, which is an alternative explanation of the pinched shape of the P–E hysteresis.[70] The experimentally observed AFE-like double hysteresis loops in the P–E curve indicate that an electric field-induced phase transition between AFE and FE phases occurs. According to the theory, the total energy of AFE t-phase is lower than that of FE oIII-phase by only ≈1 meV per formula unit (0.1 kJ mol^{-1}) for the case of ZrO$_2$.[21] For the case of HfO$_2$, however, the total energy of FE oIII-phase was much smaller than that of the AFE t-phase by ≈23 meV per formula unit (2.2 kJ mol^{-1}). Hence, the FE oIII-phase is more energetically stable than the AFE t-phase, which explains well the emergence of the AFE phase only in the Zr-rich compositions in Hf$_{1-x}$Zr$_x$O$_2$ films.[21] This also suggests that the doping of HfO$_2$ into AFE ZrO$_2$ is expected to reduce the energy of the FE oIII-phase, resulting in an easier transition from the AFE to FE phases by applying an external bias, which actually occurred with thin films of HfO$_2$–ZrO$_2$

Materials
Views
www.MaterialsViews.com

ADVANCED
MATERIALS
www.advmat.de

PROGRESS REPORT

solid-solution.[32,46] Moreover, the energy difference could be further decreased when the compressive stress is applied along the a- and b-axis of the t-phase.[21] In the paper, however, the total energy instead of the free energy was calculated and the m-phase was still found to have the lowest energy. Nonetheless, Reyes-Lillo et al. mentioned that the formation of the stable m-phase might be suppressed by other factors such as surface energy effects.[21]

An accurate investigation of the energy landscape of the polymorphs, including surface effects, was done by Materlik et al.[69] With the density functional calculations, the free energy of the relevant ZrO_2, $Hf_{0.5}Zr_{0.5}O_2$ and HfO_2 phases, depending on the stress and temperature, were calculated, along with the surface energy contributions depending on the average grain size (D_{ave}). The required values for the surface energy density were estimated from available data. Because the free energy of the polar oIII-phase is lower than that of the t-phase and the surface energies of the t-phase and oIII-phase are less than or similar to those of the m-phase, the free energy of the oIII-phase could be the lowest for the polycrystalline $Hf_{0.5}Zr_{0.5}O_2$ material with a very small D_{ave}. For higher temperature or larger Zr content, the t-phase was slightly more favored. An applied electric field favors the oIII-phase relative to the t-phase and a nearly barrierless field-induced-phase-transition occurs.[21] In the paper, furthermore, the effects of oxygen vacancies on a phase stability are calculated. Such defects favor the t-phase and oIII-phase over the m-phase, amplifying the surface effect.

2.2. Experimental Works

2.2.1. Identification of FE Phase

Based on the computational calculations, it is highly plausible that the origin of the ferroelectricity in doped HfO_2 films is the oIII-phase formation. However, experimentally identifying the oIII-phase with a conventional X-ray diffraction technique is highly challenging, especially in thin films.[29,45,46] This is mainly due to the fact that the lattice parameters of the oIII- and t-phases of the (doped) HfO_2 and ZrO_2 are almost identical, which can be easily understood from the structural symmetry between the phases, as shown in Figure 1b. Moreover, generally small D_{ave} and possible co-presence of different phases with random orientations in thin films with t_f of ≈10 nm made the diffraction pattern very complicated, with broadened peak shapes. While the glancing incidence X-ray diffraction (GIXRD) is favorable for increasing the intensity of diffracted X-rays, this is generally not sufficient to evidently and quantitatively
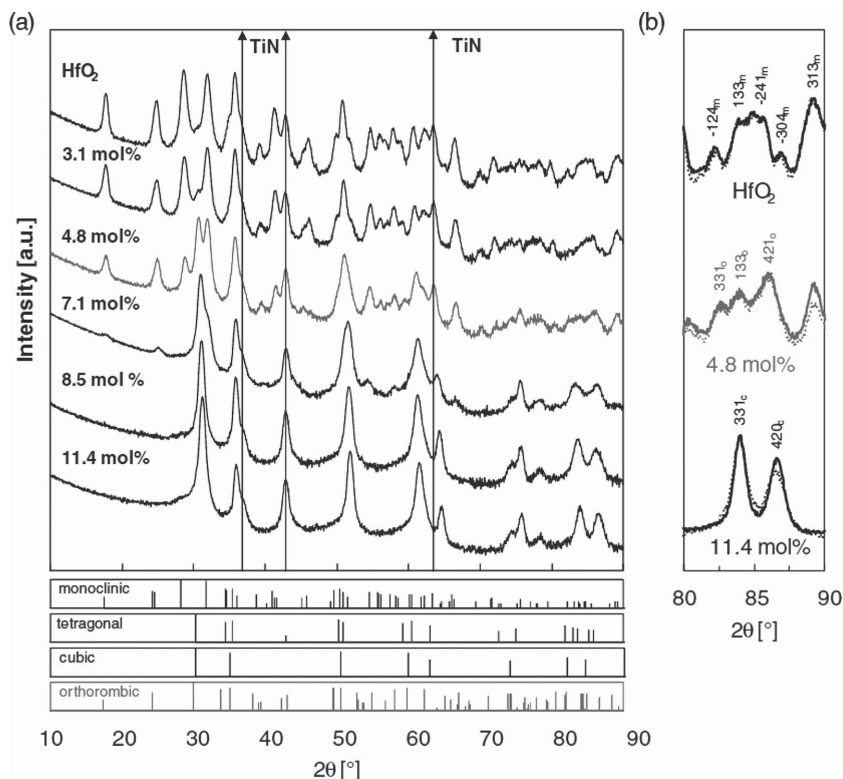

Figure 2. a) GIXRD diffractograms for Al-doped HfO_2 films having different doping concentrations. A monoclinic-to-cubic phase transition is clearly visible for increasing Al content. The powder diffraction patterns as well as the calculated orthorhombic III reference pattern are shown below the diffractograms. b) Enlarged 2θ scans from 80° to 90° for paraelectric HfO_2 containing no Al, ferroelectric HfO_2 containing 4.8% Al, and paraelectric HfO_2 containing 11.8% Al. The diffractogram of the ferroelectric composition shows a triplet which would not be expected for monoclinic, tetragonal, or cubic phases. The dotted lines show results for PDA sample of the same composition. Reproduced with permission.[46]

identify the phases in the HfO_2 based thin films. Despite these difficulties, Böscke et al. reported a clear difference between the GIXRD patterns of m-, t- and oIII-phase in the Si-doped HfO_2 films.[29] After that, the diffraction pattern in the 2θ range of 80–90° was also adopted to identify the oIII-phase for the case of Y-, Gd-, Al- and Zr-doped HfO_2.[37,43,46,48] Among these results, it is believed that the report by S. Müller et al. on the Al-doped HfO_2[46] was the most systematic and clear, in showing the difference of the X-ray diffraction (XRD) pattern of the t- and oIII-phase. **Figure 2** shows the GIXRD diffractograms for the Al-doped HfO_2 films with various Al-doping concentrations from 0 to 11.4%, with the reference diffraction patterns, which were deposited by an ALD process and post-annealed at temperatures of 800–1000 °C for crystallization. The pure HfO_2 is the m-phase, whereas the phase transition from the m- to oIII- to c-phase with increasing Al contents can be clearly observed.[46] Especially, the data in the 2θ ranges of 80–90° of HfO_2 with different Al-doping concentrations are enlarged in Figure 2b, which showed the clearest differences over the entire 2θ range. They observed the diffraction peaks from (331), (133), and (421) planes of the oIII-phase in that region, which were distinguishable from the diffraction peaks of the t- and m-phases.[46] In contrast, Park et al. recently reported that the GIXRD data in the 2θ range of 27–33° could be very useful to quantitatively

identify not only the types of the involving phases but also their relative portions. This could be done by utilizing the deconvolution technique, assuming Gaussian shapes of the constituent peaks from the various phases for the $Hf_{1-x}Zr_xO_2$ films over the wide composition and t_f ranges.[39]

In contrast, in the recent report on Y-doped HfO_2 films grown by a sol-gel solution process, Starschich et al. could not observe any evidence for the formation of the oIII-phase even in the 2θ range of 80–90°.[45] They could only observe the diffraction peaks from the c-phase which is generally known for Y-doped HfO_2 structure.[45] The thickness of the Y-doped HfO_2 film in the study (up to ≈70 nm) was the largest among the reported results, which might be appropriate for the structural analysis using XRD. However, they clearly showed the FE-characteristic P–E hysteresis curves. This will be further discussed in the next section. Certainly, a clear phase identification needs further improvements.

2.2.2. Effect of Film Thickness and Grain Size

The FE properties depend strongly on the grain formation process, and it is generally known that t_f and temperature budget affect the average D_{ave}. So far, it seems critical that the dielectric layer is deposited in the amorphous phase and crystallized in a later annealing step. Böscke et al. explained that capping a top electrode avoids shearing and volume expansion of the unit cell during the crystallization process, and hence reduces the formation of the m-phase.[31] Si and Gd doped films showed stable P_r values in the t_f range accessible by ALD deposition (5–30 nm).[71,72] Yurchuk et al. first reported a decrease of P_r for higher t_f, but the thicker films were crystallized during the deposition, which resulted in the augmented portion of the m-phase.[34] Similar results were extracted for $Hf_{0.5}Zr_{0.5}O_2$ layers.[38] Here, the deposition temperature was very close to the crystallization temperature, which again favored the higher quantities of the m-phase grains and the lower P_r values for the thicker layers.

Park et al. examined the effect of t_f on the FE properties of the $Hf_{0.5}Zr_{0.5}O_2$ films.[40] They tested the $Hf_{0.5}Zr_{0.5}O_2$ films with various t_f (5.5–25 nm) and annealing temperature (400–800 °C). When the t_f was ≈10 nm, the P_r of the $Hf_{0.5}Zr_{0.5}O_2$ films was the largest (≈15 µC cm^{-2}), whereas the P_r decreased to ≈12 and ≈5 µC cm^{-2} when the t_f increased to 17 and 25 nm, respectively. This could be understood from the fact that the portion of the m-phase increased as the t_f increased.[39] The effect of the t_f on P_r variation could be ascribed to the change in D_{ave} of the $Hf_{0.5}Zr_{0.5}O_2$ films. It has been well known that the polymorphism of polycrystalline HfO_2 and ZrO_2 is governed by the size effects, especially when the D_{ave} is <≈100 nm.[73–78] The critical D_{ave} to obtain a t-phase is known to be ≈4 and ≈32 nm for HfO_2 and ZrO_2, so the critical D_{ave} of $Hf_{0.5}Zr_{0.5}O_2$ is estimated as ≈18 nm, from interpolation based on Vegard's law.[75,76] When the D_{ave} of the HfO_2-based films is maintained below their critical size, the t-phase could be induced by the surface or grain boundary effect. The specific surface energy of the oIII-phase is not experimentally known, but it can be assumed that this could contribute to the oIII-phase stabilization. This could be a mechanism complementary to the appropriate asymmetric stress (see Sections 2.1 and 2.2.3) which is known to result in the oIII-phase. The effect of D_{ave} on phase stability has been discussed thoroughly by Materlik et al.[69] It is evident that achieving the D_{ave} smaller than the critical size so as not to induce the formation of stable m-phase is a pre-requisite to achieve the FE or AFE behaviors from the HfO_2-based thin films. It is also evident that the D_{ave} is quite dependent on the t_f when the $Hf_{1-x}Zr_xO_2$ films (and other doped HfO_2 films, too) were grown by ALD; the thicker the film, the higher the portion of a m-phase and the lower the FE performance.[34,39] So, the maximum t_f for feasible FE and AFE performance has been limited to <≈20 nm for $Hf_{1-x}Zr_xO_2$, and the value is at least ≈30 nm for Si- or Gd-doped HfO_2. However, this may not necessarily be the case if another deposition technique was adopted. Starschich et al. recently reported that the Y-doped HfO_2 films could show a feasible FE performance up to a t_f of 70 nm when the film was grown by chemical solution deposition (CSD).[45] Although the origin of the phenomenon was not exclusively elucidated, the step-by-step process of coating–annealing–crystallization, which produces ≈7 nm-thick layers per step, may induce perturbation of a columnar grain growth up to the total t_f, and the FE performance could be retained up to such a large t_f. The desirable aspects of such thick FE Y-doped HfO_2 films were that they were very useful to clearly identify the phase, and obtain a clear piezoelectric displacement response signal in laser interferometer measurements, which is direct evidence for the involvement of FE distortion of the crystal.[79] Interestingly, however, both the 18 nm and 70 nm-thick films showed a clear crystal structure of the c-phase without any oIII-phase, although the laser interferometer measurements revealed that the films were piezoelectric, as expected for FE materials. A phase change during the field cycling might be the reason for this effect. Another critical point of this work is that Pt was adopted for the bottom and top electrode for such a solution-based process, which resulted in undesirable results for ALD-based $Hf_{1-x}Zr_xO_2$ films.[40] Therefore, there is still a large amount of work to be performed to fully understand the underlying principles for the FE performances and phase transitions.

2.2.3. Effect of Asymmetric Stress

The origin of the formation of an unexpected FE phase was systematically examined for $Hf_{0.5}Zr_{0.5}O_2$ films by Park et al. from the view point of an asymmetric stress exerted during the film growth.[40] From the available knowledge on the crystalline structures of various phases in HfO_2 and ZrO_2, they examined the c/a ratio of the t-phase and the 2b/(a+c) ratio of the oIII-phase of ZrO_2 and HfO_2 (in the bulk phase). It should be noted that the c-axis of the oIII-phase, which is the direction of P_r, has the shortest lattice parameter, whereas the nonpolar b-axis has the longest. For the case of the t-phase, on the other hand, the c-axis has the longest lattice parameter, so the c-axis of the t-phase would be the b-axis of the oIII-phase during the phase transition. It could be understood that the 2b/(a+c) ratios of the oIII-phases (of both HfO_2 and ZrO_2) are higher than c/a ratios of the t-phases.[37,39,63,80–83] In addition to the difference in the ratio for the oIII- and t-phases, there was another subtle difference between the HfO_2 and ZrO_2, which could play the crucial

role in understanding the strain-induced phase transition behavior correctly: the difference between the 2b/(a+c) ratio of the oIII-phase and c/a ratio of the t-phase were higher for ZrO_2 (1.015–1.016 for the t-phase and 1.036 for the oIII-phase, differed by ≈2%) than that of HfO_2 (1.028–1.029 for the t-phase and 1.038 for the oIII-phase, differed by ≈1%).[38,40,64,80–83] Therefore, for the transition from the t-phase to oIII-phase, a much higher stress (≈4 GPa) would be needed for ZrO_2 than that needed for HfO_2, and this is the reason why Zr-rich $Hf_xZr_{1-x}O_2$ films can hardly be FE; Zr-rich $Hf_xZr_{1-x}O_2$ films generally remained in t-phase, making them more vulnerable to being AFE.[21]

For the case of HfO_2, on the other hand, it is very difficult to prevent the formation of the stable m-phase due to its much smaller critical D_{ave} for the transition to t-phase (≈4 nm).[76] So, the FE oIII-phase can be hardly formed despite the smaller strain necessary to induce the transition into the oIII-phase. Therefore, Hf-rich $Hf_xZr_{1-x}O_2$ films generally remained in the m-phase, which merely works as a high-k dielectric layer. A feasible FE phase was usually achieved from the composition near a Hf:Zr ratio of approximately 0.5:0.5.[37] Although these considerations simply reflect the possible strain from the difference in the lattice parameters of the t- and oIII-phases, these assertions are actually very similar to the theoretical considerations of the energy suggested by Reyes-Lillo et al.[21] They suggested that the in-plane compressive stress in the a-b plane of a t-phase is the origin of the formation of the unexpected FE oIII-phase, which might induce the tensile strain along the c-axis of the t-phase.[21] The polarization component resulting from this mechanism, however, is parallel to the film surface and not measurable. In thin film growth, in-plane tensile stress (also strain) could be induced by several mechanisms, but for the case of ALD $Hf_{0.5}Zr_{0.5}O_2$ films, the zipping stress was suggested to be the appropriate reason for inducing the required stress state in the film.[40,84,85] Zipping stress is the stress imposed on the whole film when the neighboring nuclei just start to touch each other and "zip" the grain (or even amorphous cluster) boundaries.[84,85]

For this mechanism to operate, the crystallographic orientations of $Hf_{0.5}Zr_{0.5}O_2$ grains are another critical factor. Since the growing nuclei are supposed to have t-phase structure prior to the zipping, and because of the surface energy effect, there must be several variations in the resulting strain states after the

zipping, according to the original crystallographic directions of the nuclei. Using the in-plane stress condition of the film, Park et al. could calculate the strain along the a-,b-, and c-axis of the grains of various orientations using the in-plane stress conditions of the thin film.[40] As a result, the 110-orientation was the most favorable for the formation of the oIII-phase from t-phase, whereas the 111-orientation was the worst, since almost equivalent strains were formed along the a-, b-, and c-axis (none of the a-, b-, and c-directions can be tensile while other direction is compressive).[40] This was indeed the case in an experiment on the ALD $Hf_{0.5}Zr_{0.5}O_2$ film on the highly 111-oriented Pt electrode, which resulted in the highly 111-oriented $Hf_{0.5}Zr_{0.5}O_2$ film.[40] Even though the 111-oriented $Hf_{0.5}Zr_{0.5}O_2$ film fulfilled the aforementioned conditions for the emergence of the FE property (D_{ave}, stress, and composition), the highly 111-oriented, 9.2 nm-thick $Hf_{0.5}Zr_{0.5}O_2$ film showed neither FE nor AFE properties (**Figure 3**a).[40] In contrast, the $Hf_{0.5}Zr_{0.5}O_2$ film simultaneously grown on a TiN electrode showed no preferred orientation, and feasible P–E hysteresis, revealing the FE performance (Figure 3b).[40] As seen in Figure 3c, the in-plane strain in $Hf_{0.5}Zr_{0.5}O_2$ films deposited on the Pt bottom electrode was as large as that on the TiN bottom electrode.[40] Therefore, the formation of the FE oIII-phase also depends heavily on the film orientation, in addition to the D_{ave}, which is determined by the t_f for the case of ALD. It is also noted that the FE (and also AFE) performance could be further improved by an appropriate control of the film growth direction, perhaps by adopting different substrates and growth methods/conditions, because the present level of FE performance was mostly achieved from randomly oriented films, which also contain non-FE phases.

2.2.4. Effect of Top Capping Electrode and Annealing

TiN has been known to be the most commonly used electrode material for FE HfO_2-based films. In most previous reports, FE HfO_2-based films were sandwiched between top and bottom TiN electrodes.[29–34,36–44,46–50] The capping top electrodes, including TiN, is known to be critical for the ferroelectricity of the HfO_2-based films. Böscke et al. compared the GIXRD pattern of Si-doped HfO_2 films, crystallized before and after the deposition of the upper TiN capping layer.[29] When the film was annealed before the deposition, the intensities of the
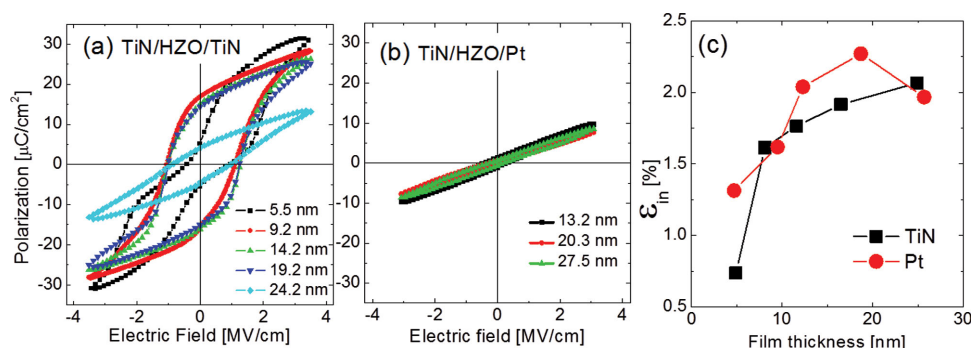

Figure 3. The polarization–electric field hysteresis curves of $Hf_{0.5}Zr_{0.5}O_2$ films with various thickness on a) TiN and b) Pt electrode. The top electrode was TiN for both of them. c) The variations in in-plane strain of $Hf_{0.5}Zr_{0.5}O_2$ films as a function of film thickness. Reproduced with permission.[40] Copyright 2014, AIP Publishing LLC.

diffraction peaks from the m-phase were much larger, compared to those from the oIII-phase.[29] In contrast, the diffraction peaks from the m-phase could hardly be observed for the case of the films crystallized with the TiN capping layer.[29] They reported that the TiN capping layer could act as a mechanical confinement, which is necessary to prevent the volume expansion and shearing of the monoclinic unit cell. This could be done by clamping the film mechanically, and thus, suppressing the formation of the non-FE phases.[29] However, this could be one of several factors and not the main cause for the emergence of ferroelectricity, as other experiments have shown. Although not clearly elucidated, this might be related to the suppression of ion migration on the film surface during the annealing, which could have induced the grain growth, and accompanying m-phase formation. After Böscke et al., most of the HfO$_2$-films were prepared with the presence of the TiN capping layer. For most of the doped HfO$_2$ films, the films crystallized without the capping layer showed relatively smaller P$_r$ values than those with the capping layer.[43,46,48]

Compared to the Si-doped HfO$_2$, Hf$_{0.5}$Zr$_{0.5}$O$_2$ films, in contrast, were less influenced by the TiN capping layer. Park reported that the P$_r$ values of Hf$_{0.5}$Zr$_{0.5}$O$_2$ capacitors with and without the TiN capping layer were almost equivalent when the deposition process of the TiN layer was carefully optimized.[85] This might be related to the lower annealing temperature for the case of Hf$_{0.5}$Zr$_{0.5}$O$_2$ (400–600 °C), compared with the Si-doped HfO$_2$ (1000 °C).[36–43,85] The low annealing temperature did not induce any significant grain growth and thus the m-phase formation was hindered despite an absence of the capping TiN layer. Lomenzo et al. recently reported that Ir can also work as a capping layer instead of TiN on Si-doped HfO$_2$ films.[35] In this experiment, they used heavily-doped Si and Ir as the bottom and top electrode, respectively.[35] This TiN-free capacitor also showed robust ferroelectricity, proving that TiN is not the only feasible bottom electrode material for Si-doped HfO$_2$ films. Schenk et al. reported the improved P$_r$ values by replacing the TiN electrode with TaN for Gd:HfO$_2$. Here, the P$_r$ value increased from 20 μC cm^{-2} to 30 μC cm^{-2} by changing both electrodes.[86] Meanwhile, the top electrode, especially a conducting oxide electrode, has been a critical asset to improve the reliability of a FE PZT layer, given the fact that the bottom electrode can be hardly replaced by other materials for the given process conditions to achieve the desired crystalline structure.[87,88] Park et al. have attempted to improve the endurance property of the Hf$_{0.5}$Zr$_{0.5}$O$_2$ capacitor by replacing the TiN top electrode with RuO$_2$ which is well known to improve the endurance of conventional FE materials such as PZT.[41] However, during the crystallization process, the RuO$_2$ was reduced, due to the oxygen scavenging effect of the bottom TiN layer, and this seriously degraded the FE properties of Hf$_{0.5}$Zr$_{0.5}$O$_2$ capacitors.[41] Moreover, the TiN layer can also work as a barrier for the H incorporation during forming gas annealing although HZO itself is generally less likely to degrade by hydrogen gas annealing than other conventional FE materials.[38]

To summarize this section, it is believed that the TiN and possibly the TaN capping layers generally improved the FE properties of HfO$_2$-based films especially when the crystallization was performed at high temperature (800–1000 °C).[43,46,49]

An Ir capping layer can work in a similar way.[35] So far, the FE HfO$_2$-based films sandwiched by the top and bottom TiN electrode appear to be the best structure for actual applications. Careful control of the oxygen scavenging effect by the TiN is necessary when RuO$_2$ forms one of the electrodes.[41] TiN is believed to be an attractive electrode material for HfO$_2$-based films due to its role as a barrier layer against H incorporation, its Si-compatibility, and the cost effectiveness.[38]

3. Effects of Dopants

As already mentioned in the introduction, various dopants such as Si, Al, Zr, Y, Sr, La, and Gd were reported to induce ferroelectricity in HfO$_2$ films.[29,40–50] This is due to the formation of the t-phase or c-phase which brings the higher ε_r to the high-k gate dielectrics, the prerequisite for the final transition to the oIII-phase. In this section, FE and AFE properties of HfO$_2$ films with various dopants are summarized. This topic has been already reviewed by Schröder et al.,[30,90] but current reports on dopant effects supplement the previous knowledge. Above many other important dopants, Si and Zr are discussed more in detail in this paper, since they have been most reported.

3.1. Si-Doped HfO$_2$ Films

FE properties of Si-doped HfO$_2$ were first reported in 2011, and were mostly studied by the Namlab/Fraunhofer CNT collaboration.[29,31–35,71,72] AFE properties of the Si-doped HfO$_2$ were also reported in the same reports, but most of the work focused on the FE properties. Si is the fundamental material in semiconductor industry, so adopting Si as a doping material would be preferred according to process maturity and contamination control in semiconductor mass-production.

Si is a tetravalent material, and its atomic radius (110 pm) is ≈29% smaller compared to that of Hf (155 pm).[91] Due to the smaller atomic radius of Si, the volume of the unit cell decreases with increasing Si-doping concentration.[30,90] Si-doping is known to stabilize the t-phase of HfO$_2$, and the maximum solubility of Si in HfO$_2$ is known to be ≈9%.[92] When the atomic ratio of Si and Hf is 1:1, HfSiO$_4$, which is called Hafnon, is known to be stabilized, but this phase is hardly observed in studies on Si-doped HfO$_2$ films.[93] **Figure 4**a shows the comparison of P$_r$ values for two different t$_f$ of 12 and 36 nm,[71,72] while Figure 4b shows the change in ε_r of the 12nm-thick film as a function of the Si-concentration. For both thicknesses, the maximum polarization is reached at ≈3.8% Si, followed by an AFE region between 5–8% Si, before the material again solely behaves in a paraelectric manner at higher Si-concentrations. One indication for the transition is the position of the (111) oIII-phase or (011) t-phase peak of the XRD patterns (Figure 4c). The position shifts from ≈ 30.6° for the FE oIII-phase to 30.8–31.3° for the AFE t-phase, indicating an expansion of the lattice. The thicker 30 nm films enlarge more than the 10 nm layers. Along with the phase transformation, the ε_r of the material increases from ≈20 for the m-phase to ≈38 for the t-phase.[32,71] The P$_r$ values for the 10–30 nm t$_f$ range reach
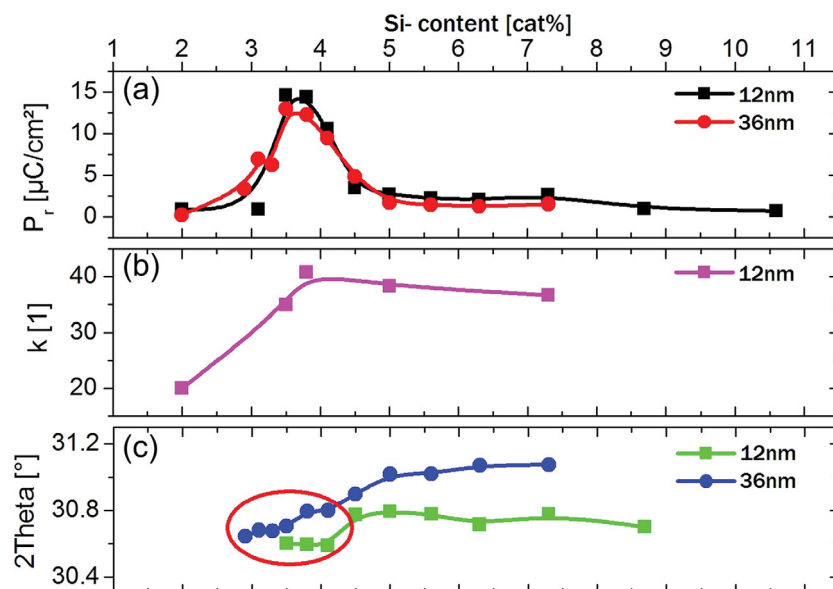
Figure 4. a) Remanent polarization of 12 nm and 36nm Si-doped HfO₂ for different Si content. b) Change of the dielectric constant for different Si concentration. c) Change of the (111o /011t) XRD peak position for 12 and 36 nm thick Si-doped HfO₂ indicating a change of the phase from orthorhombic to a tetragonal lattice structure. Samples with a 2θ value of about 30.6° show highest Pr values.

a similar value of about 13–15 µCcm⁻², and only slightly lower values are reported at 5 nm t_f (10 µC cm⁻²).[71] For this dopant, stable P_r values are expected, as long as the anneal conditions cause a similar grain formation, resulting in certain dopant conditions in the material. Richter et al.[71] found a clear correlation between the dopant concentration and the field cycling behavior for 10 nm-thick films. Between 2–3% doping concentrations, the film is paraelectric, and ferroelectricity appears during the field cycling, as shown in the hysteresis measurements (see Figure S1). For higher dopant contents between 3.5–4.5% the film is initially AFE-like, but the FE curve shape arises at the expense of the AFE feature during the field cycling. Beyond 4.5% a clear stable AFE behavior is detected during the cycling.[29,30,71,72] For higher Si-concentrations, the field required to induce FE polarization in theses AFE layers increases. Piezoresponse force microscope (PFM) measurements revealed a complete polarizability of the FE layer.[30,94] Rectangular patterns could be polarized in the surface in both polarization orientations. The typical domain size was determined to be 100–300 nm. The change of the ALD sequence of SiO₂ and HfO₂, as well as the ALD cycle ratio of SiO₂ and HfO₂, strongly affects the FE properties of Si-doped HfO₂ films. Lomenzo et al. reported that the P_r of Si-doped HfO₂ films with doping concentration of ≈5.5–5.7% decreased with increasing inhomogeneity of Si dopants, meaning that the portion of the non-ferroelectric phases increased.[95] Zhou et al. found that the leakage current density of 10 nm-thick Si-doped HfO₂ film was smaller than 4 × 10⁻⁵ A cm⁻² even under a very large electric field of 3 MV cm⁻¹.[32] The cycling reliability of Si-doped HfO₂ capacitors sandwiched between the TiN top and bottom electrodes was examined by J. Müller and coworkers.[96] The 10 nm-thick

Si-doped HfO₂ film could endure up to 10¹⁰ cycles with the cycling pulse height of 2 MV cm⁻¹, which is not large enough to induce the saturated P_r values. P_r value at this field strength was only ≈7 µC cm⁻², which degraded to 2 µC cm⁻² after field cycling 10¹⁰ times.[96] In the retention test, on the other hand, both positive and negative P_r states did not decrease after up to 10³ hours at 125 °C.[96] Therefore, the endurance of Si-doped HfO₂ film needs improvement for semiconductor memory applications. One of the general issues with doped HfO₂-based FE layers is its very high coercive field (E_c) of ≈1 MV cm⁻¹. Although the coercive voltage (V_c) could be as small as ≈1 V at a t_f of 10 nm, this required sufficiently high drive field (≈3 MV cm⁻¹) to invoke the full P_r, which imparts significant reliability problem during the endurance test. Therefore, the intrinsic endurance cycle of these new FE materials has not really been explored yet, although the high bonding energy between the oxygen and constituent metal ions may result in inherently better reliability than conventional FE materials.[39] The reliability characteristics of a memory device using Si-doped HfO₂ will be presented later, in Section 4.1.

3.2. Hf₁₋ₓZrₓO₂ Films

ZrO₂ and HfO₂ show very similar physical and chemical properties. Zr is tetravalent, and its atomic radius (155 pm) is almost equivalent to that of Hf (155 pm).[91] They have almost equivalent crystal phases with almost identical lattice parameters. Due to their similarities, the HfO₂–ZrO₂ system forms single phase solid solution over the entire composition range.[37] The HfO₂ and ZrO₂ are used as standard materials for the high-k gate dielectric layer in advanced metal-oxide-semiconductor field effect transistors (MOSFET) and capacitors for DRAM, meaning that they are highly mature materials in the semiconductor industry.[60] J. Müller et al. first reported the FE property of Hf₀.₅Zr₀.₅O₂ films with a typical P_r value of 16 µC cm⁻² and E_c of 1 MV cm⁻¹.[36] For the Hf- and Zr-rich compositions, normal dielectric ($ε_r$ = 15–20) and AFE properties were achieved.[37] **Figure 5**a shows the P–E hysteresis and $ε_r$–E curves of the Hf₁₋ₓZrₓO₂ (x = 0, 0.3, 0.4, 0.5, 0.7, and 1.0) films. Figure 5b shows that possible leakage current through the thin FE and AFE layers can hardly influence the P–E hysteresis shapes.[37] As seen in the upper panel of Figure 5c, the maximum P_r value of ≈16 µC cm⁻² could be achieved for the case of the Hf₀.₅Zr₀.₅O₂ films.[37] The bottom panel of Figure 5c shows that the $ε_r$ value increases with increasing ZrO₂ content and decreasing m-phase portion. Compared to the Si-doped HfO₂, Hf₁₋ₓZrₓO₂ films could be crystallized at the lower crystallization temperature (400–600 °C).[36–42,51–54] Such a low annealing temperature compared to Si-doped HfO₂
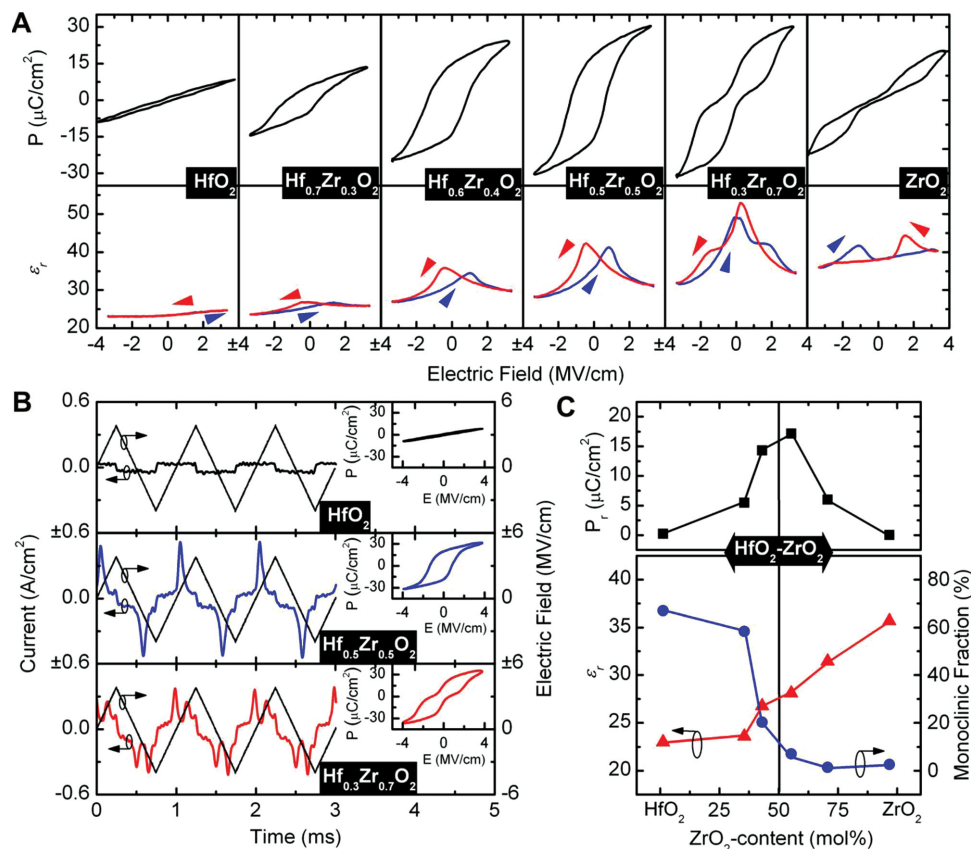
Figure 5. a) Polarization–electric field (top row) at 1 kHz and small signal dielectric constant (ε_r)–electric field (bottom row) curves of 9 nm-thick $Hf_{1-x}Zr_xO_2$ films sandwiched by TiN top and bottom electrode. b) Current response to a triangular voltage excitation reveals polarization switching to be cleanly separable from leakage current contributions at high fields. c) P_r, ε_r, and m-phase fraction in the $Hf_{1-x}Zr_xO_2$ films with respect to the mixing ratio of the oxides. With increasing ZrO_2 content, the ε_r increases due to a reduction in m-phase fraction, whereas the remanent polarization is maximized in the transition region. Reproduced with permission.[37] Copyright 2012, American Chemical Society.

could be a strong merit of $Hf_{1-x}Zr_xO_2$ films for the integration process. The ε_r of ≈10 nm-thick FE $Hf_{0.5}Zr_{0.5}O_2$ layer was ≈28–33, whereas that of AFE $Hf_{0.3}Zr_{0.7}O_2$ was ≈32–42.[37,39,51] The leakage current density was ≈1.0×10^{-4} A cm^{-2} and ≈2.0×10^{-4} A cm^{-2} at 3 MV cm^{-1} for ≈10nm-thick $Hf_{0.5}Zr_{0.5}O_2$ and $Hf_{0.3}Zr_{0.7}O_2$ films, respectively.[39,51] Shimizu et al. recently reported the FE properties of $Hf_{0.5}Zr_{0.5}O_2$ films deposited using metal organic chemical vapor deposition (MOCVD).[97] They carefully optimized annealing conditions for 16 nm-thick $Hf_{0.5}Zr_{0.5}O_2$ films sandwiched between Ir top and bottom electrodes, and reported a P_r of ≈14 μC cm^{-2}, which was slightly smaller than that of the ALD-deposited $Hf_{0.5}Zr_{0.5}O_2$ films.[97] This result was the first to prove that the FE properties can be observed in doped HfO_2-based films deposited using MOCVD. The leakage current density of $Hf_{1-x}Zr_xO_2$ films was slightly larger than that of Si-doped HfO_2 films. The endurance characteristics of FE $Hf_{0.5}Zr_{0.5}O_2$ films were examined, and 5.5 nm and 10 nm-thick $Hf_{0.5}Zr_{0.5}O_2$ films could endure up to 10^9 and 10^8 times field cycling, respectively, with a cycling field strength of 3 MV cm^{-1}.[41] The endurance property of the $Hf_{0.5}Zr_{0.5}O_2$ films was better than that of the Si-doped HfO_2 films with cycling field strength of 3 MV cm^{-1}. According to the previous report by J. Müller et al., the positive and negative P_r values did

not decrease after 10^5 seconds in their retention test.[36] To conclude, $Hf_{0.5}Zr_{0.5}O_2$ films are also believed to be as promising as Si-doped HfO_2 films.

3.3. Other Dopants

The interesting point from the FE properties of Y-doped HfO_2, first reported in 2011 by J. Müller et al,[43] is its high P_r of ≈24 μC cm^{-2} when the Y-doping concentration was 2.3–5.2%. **Figure 6**a shows the polarization–voltage (P–V) hysteresis of the Y-doped HfO_2 films with various doping concentrations (2.3–12.3%) annealed with (upper panel) and without (bottom panel) the TiN top electrode, respectively. Y is a trivalent material, and its atomic radius (180 pm) is ≈16% larger than that of Hf (155 pm).[91] It is well known that Y can stabilize the c-phase of HfO_2 films, and the FE phase is formed at the morphotropic phase boundary of the m- and c-phase.[43–45] Interestingly, the FE Y-doped HfO_2 films could be deposited via various deposition techniques, such as ALD,[43] sputtering,[44] and CSD.[45] For the Y-doped HfO_2 deposited via sputtering, the Y doping concentration for the FE properties with a large P_r was 0.9–1.9%, which was much lower compared to that of the ALD films.[44]
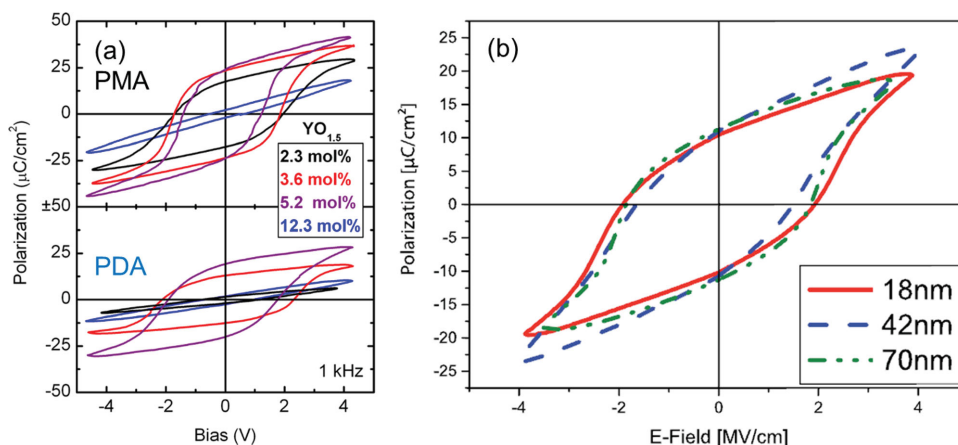
Materials
Views
www.MaterialsViews.com

ADVANCED
MATERIALS
www.advmat.de

PROGRESS REPORT

Figure 6. a) The polarization–voltage hysteresis curves of 10 nm-thick Y-doped HfO_2 films with various doping concentrations sandwiched by TiN top and bottom electrode treated with post-metallization annealing (PMA, upper panel) and post-deposition-annealing (PDA, bottom panel), respectively. The films were deposited via ALD. Reproduced with permission.[43] Copyright 2011, AIP Publishing LLC. b) The polarization–electric field hysteresis curves of Y-doped HfO_2 films with the thickness of 18–70 nm. The films were deposited via chemical solution deposition. Reproduced with permission.[45] Copyright 2014, AIP Publishing LLC.

The maximum P_r of the sputtering-deposited 12 nm-thick Y-doped HfO_2 films was ≈15 $\mu C\ cm^{-2}$, which is ≈37% smaller compared to that of the ALD-deposited films.[44] The E_c of the sputtering deposited film (1.5 MV cm^{-2}) was ≈25% larger than that of the ALD-deposited films (1.2 MV cm^{-1}).[43,44] Perhaps the most interesting point of this report is that the pure HfO_2 film could show the FE hysteresis in its P–E curve, which is the first report showing the FE property from non-doped (or, not intentionally doped) HfO_2 films.[44] This might be correlated with the highly non-equilibrium and energetic particle bombardment during the reactive sputtering process of the sputtered HfO_2 film, but further study is definitely necessary to fully explore this possibility.[44] Starschich et al. reported the FE properties of the Y-doped HfO_2 films deposited via CSD.[45] The doping concentration was 5.2%, which was almost equivalent with the previous report on the ALD-deposited film, and the maximum P_r was ≈13 $\mu C\ cm^{-2}$.[45] Figure 6b shows the P–E hysteresis of the Y-doped HfO_2 films with various t_f (18, 42, and 70 nm) deposited via CSD.[45] As aforementioned, the most notable from this work was that the FE properties of these CSD-deposited film were not degraded even when the t_f increased up to 70 nm.[45]

FE and AFE properties of Al-doped HfO_2 were first reported in 2012 by S. Müller and coworkers.[46] Al is a trivalent material, and its atomic radius (125 pm) is ≈19% smaller than that of Hf.[91] The maximum P_r of 16 nm-thick Al-doped HfO_2 film was ≈6 $\mu C\ cm^{-2}$ with a doping concentration of 4.8%.[46] However, a maximum P_r value of ≈16 $\mu C\ cm^{-2}$, which is comparable to that of other FE films, has been recently reported after optimization.[47] The E_c of Al-doped HfO_2 was ≈1.3 MV cm^{-1}, which was slightly larger than that of the Si- and Zr-doped HfO_2 films.[46] The ε_r of the FE Al-doped HfO_2 was 30, which was comparable to those of Si-, and Zr-doped HfO_2 films.[46] When the doping concentration increases to 8.5%, the AFE distortion of P-E hysteresis could be observed, but the maximum polarization of AFE films was relatively smaller than that of the AFE HfO_2 films with other dopants. Al leads to a paraelectric-ferroelectric-antiferroelectric-paraelectric phase transition with increasing Al-concentration, along with a monoclinic-orthorhombic III-tetragonal-cubic phase transition.[46]

FE properties of Gd-doped HfO_2 were first reported in 2012.[48] Gd is a trivalent material, and its atomic radius (180 pm) is ≈16% larger than that of Hf.[91] It has been reported that the doping of Gd into HfO_2 could stabilize the metastable c-phase.[48] The maximum P_r value of the optimized FE Gd-doped HfO_2 film with doping concentrations of 2–3% was ≈20 $\mu C\ cm^{-2}$, which was almost constant for different t_f values (10–30 nm)[72,98]. Similar FE properties could be observed on Si and TaN substrates and for TaN top electrode.[98] E_c of Gd-doped HfO_2 was 1.75 MV cm^{-1} which is the second largest value among FE HfO_2 films. AFE-like hysteresis could only be observed for pristine Gd-doped HfO_2 films without field cycling.[98]

FE properties of Sr-doped HfO_2 were first reported by Schenk et al. in 2013.[49] Sr is the only divalent dopant used for FE HfO_2 films, and its atomic radius (200 pm) is ≈29% larger than that of Hf.[91] The maximum P_r of Sr-doped HfO_2 film was ≈23 $\mu C\ cm^{-2}$, which is comparable to those of other doped HfO_2 films, with the doping concentration of 4.4 mol%.[72] Its E_c was 2.0 MV cm^{-1}, the largest among doped FE HfO_2 films.[30] Interestingly, Sr-doped HfO_2 films could show FE properties within the largest range of doping concentration in both ab-initio simulations and experiments. According to the ab-initio simulation results by Schenk et al., the energy difference between the oIII- and t-phase is less sensitive for Sr-doping than Si-doping, so it is expected that the Sr-doped HfO_2 can show FE properties in a wider range of doping concentrations compared to Si-doped HfO_2. By P–E measurements, FE properties could be confirmed even with doping concentration as high as 10%.[30]

FE properties of La-doped HfO_2 were first reported by J. Müller et al. in 2013.[50] La is a trivalent material, and its atomic radius (195 pm) is ≈26% larger than that of Hf.[91] The maximum P_r of La-doped HfO_2 film was 45 $\mu C\ cm^{-2}$, which is the largest value reported to date. Surprisingly, despite its small t_f, the P_r value is even comparable to that of PZT films with a t_f of a few hundred nanometers.[55–58] Therefore, it is believed
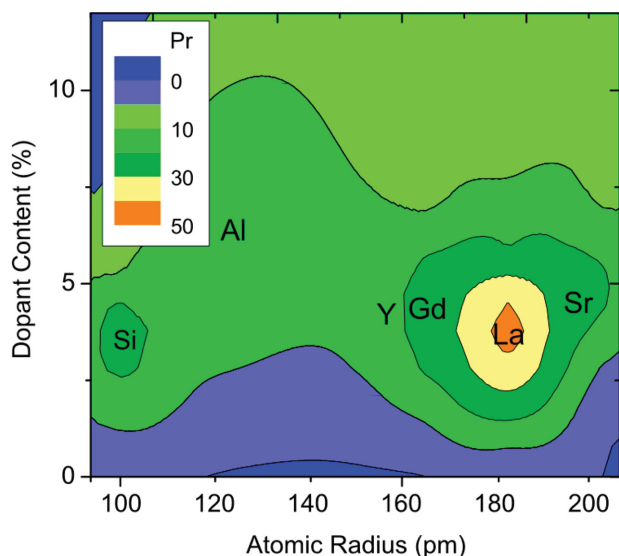
Figure 7. Contour plot of the remanent polarization as a function of crystal radius and dopant content. Reproduced with permission.[30] Copyright 2014, The Japan Society of Applied Physics.

that La-doped HfO_2 film would be very promising for memory applications, but there have been only a few reports. Other dopants like Ti and Ta did not show any FE properties, likely due to the missing m-/t- or c-phase boundaries.

3.4. Comparison of Various Dopants

Physical and chemical properties of various dopants and their effects on a phase transition are dealt in this section. Also, the resulting FE or AFE properties are presented. In the previous review paper by Schröder et al., the FE properties of HfO_2 films with various dopants were summarized as shown in **Figure 7**,[30] and additional data were summarized in **Table 1**. As seen in Figure 7, most dopants can induce feasible ferroelectricity with the P_r of 10–30 µCcm^{-2} with appropriate doping concentrations, except for the case of La (P_r > 40 µCcm^{-2}). It is difficult to find how strongly dopants affect the ferroelectricity of the doped HfO_2 films. In fact, there are many factors which can influence the P_r values of the FE films, such as the film orientation, portion of the FE phase, stress, defects, and

electrodes. Hence, the experimental P_r values in Table 1 might not be the direct measure of the ferroelectricity of the doped HfO_2 films. This also suggests that there is room for further improvement by process optimization. In principle, the maximum P_r of FE HfO_2 films could be as high as 50–60 µC cm^{-2}, from the approximate calculation based on the lattice distortion and charges of constituent ions.[25,62,68] As seen in Table 1, the atomic radius of the dopants can be smaller (Si and Al), similar (Zr), or larger (Y, Gd, La, and Sr) compared to that of Hf. Moreover, the dopants can be tetravalent (Si and Zr), trivalent (Y, Al, Gd, and La), or even divalent (Sr).[30] The only thing which the dopants have in common is that they can stabilize a t- or c-phase of HfO_2 with sufficiently high doping concentration. Lee et al. reported that the dopants smaller than Hf stabilize the t-phase of HfO_2, whereas those larger than Hf stabilize the c-phase, based on a systematic first principles study.[89] This effect of the dopant size could be well understood based on the change in the metal-oxygen bonding and resulting energy difference.[89] Therefore, it is expected that the dopant size can affect the phase transition and resulting FE/AFE properties of the doped HfO_2. Interestingly, Table 1 shows that the AFE properties of the doped HfO_2 films could be induced by dopants smaller than Hf, whereas the same property did not occur for dopants larger than Hf. The $Hf_{1-x}Zr_xO_2$ films can also show the AFE properties, but it was already reported that pure ZrO_2 films can also be AFE, based on first principle calculations.[21] Therefore, it can be noticed that the AFE properties can be observed at the morphotropic phase boundary of an oIII-phase and t-phase. To summarize, depending on the atomic radius of the dopant, different phase transitions which induce the FE and/or AFE properties were found: Zr, Si, Al monoclinic → orthorhombic III → tetragonal; Y, Gd, La, (Sr) monoclinic → orthorhombic III → cubic.

Clima et al. recently suggested that the energy barrier (E_a) for an ionic displacement for FE switching, and the resulting E_c, generally increase with the increasing atomic radius of dopants. The E_a and E_c values of the doped HfO_2 films can be seen in Table 1.[68] They also reported that the intrinsic E_c of FE HfO_2 films is estimated to be 13.4 MV cm^{-1} based on the half depolarization field argument, and E_c of the doped HfO_2 films was only 7–15% of the calculation values.[68] The much smaller experimental values could be ascribed to the domain wall dynamics due to the heterogeneous nucleation and growth of domains during the switching, which has

Table 1. The ferroelectric properties of HfO_2 films with various dopants. Data are reproduced from ref. [30] and atomic radius of dopants is taken from ref. [91]. (O: observable, X: not observable).

Dopant	Valence	Atomic radius [pm]	Theoretical P_r [µC cm^{-2}]	Experimental P_r [µC cm^{-2}]	E_c [MV cm^{-1}]	Doping concentration [%]	AFE
Si	+4	110	41	24	0.8–1.0	4	O
Zr	+4	155	50	17	1.0	50	O
Y	+3	180	40	24	1.2–1.5	5.2	X
Al	+3	125	48	16	1.3	4.8	O
Gd	+3	180	53	12	1.75	2	X
Sr	+2	200	48	23	2.0	9.9	X
La	+3	195	N/A	45	1.2	N/A	N/A

Materials
Views
www.MaterialsViews.com

ADVANCED
MATERIALS
www.advmat.de

PROGRESS REPORT

been the case for other conventional FE materials.[68] The doping concentration for maximum P_r is within the range of 2–7%, except for the special case of Zr. Reyes-Lillo et al. reported that the t-phase ZrO_2 could be an AFE material even without any doping, which is in agreement with experimental findings.[21,37] Further systematic studies on this issue via computational calculations, as well as experimental works would be beneficial to enhance overall understanding of these effects.

4. Applications

4.1. Semiconductor Memories Based on Ferroelectric Films

The idea of FE memory goes back to the year 1953, when D. A. Buck investigated the possible usage of BTO crystals for information storage.[98] The concept was based on the BTO crystal with perpendicular electrodes forming a cross point array evaporated on both sides, and was followed on by other researchers.[99,100] However, the non-rectangular hysteresis of the FE prevented the disturb-free operation of such an array, and these attempts therefore halted in the late 1950s. In the same timeframe the FeFET was proposed,[101] but could not be realized at that time. Later on, the advances in semiconductor processing solved the disturb issues by combining the storage capacitor with a MOSFET,[102] and brought about the practical realization of the FeFET.[103]

4.1.1. Capacitors of Ferroelectric Random Access Memory (FeRAM)

The disturb issues of a FE cross point array were solved in the late 1980s by introducing a MOSFET as a select device similar to DRAM.[102] The reading of the FE capacitor is accomplished by applying a defined pulse to the capacitor. If the capacitor switches, a large current corresponding to twice the remanent polarization will flow, while in the non-switching case only the flow of the displacement charge will lead to a rather low current. As a consequence, in contrast to the DRAM, the common capacitor plate line needs to be pulsed and the bit-line has to be precharged to 0 V, rather than half of the supply voltage as in the DRAM case. Other than that, the architecture is very similar to a one-transistor one–capacitor (1T–1C) DRAM.[104] The resulting memories, therefore, have the features of a RAM and are additionally non-volatile. However, conventional FEs like PZT hinder the scaling of the capacitor, which was simple for DRAM. Due to their limited t_f scaling and the lack of conformal deposition techniques,[105] a three-dimensional stacked or trench capacitor structure in commercially viable technologies, as used in DRAM arrays, has not been able to be incorporated in a memory cell with conventional FEs like PZT. Although Shin et al. recently reported the feasible FE properties of three-dimensional Ir/PZT/Ir capacitors, the total thickness of MIM stack was ≈100 nm, meaning that the minimum feature size would be even larger than 200 nm.[106] It should be noted that the state-of-the-art minimum feature size of DRAM or Flash technology is smaller than 30 nm. Moreover, even the most advanced FeRAM technology still relies on a planar capacitor

with rather large cell size of 15 F^2, where F means the minimum feature size.[104]

Therefore, FE HfO_2-based films are a very promising alternative for this application. The doped HfO_2 films are FE even at a very small t_f. They also have sufficiently large P_r, small leakage current, simpler chemical composition, and mature ALD deposition techniques.[29–50] The simpler chemical composition also eases some of the main integration challenges of classical FEs,[107,108] since the thermal budget for FE phase formation is lower and the material is much less sensitive to hydrogen.[39] On the other hand, it should be noted that the thermal budget for the crystallization process of doped HfO_2-based films depends on dopants. For the case of $Hf_{0.5}Zr_{0.5}O_2$ films, annealing at 500 °C for 30 s was enough for feasible FE properties,[35–42] whereas annealing at 600–1000 °C for 1–300s was required for Si- (1000 °C, 1–20s),[29–35] Al- (1000 °C, 20s),[46] Y- (600–1000 °C, 1–300s),[43–45] Gd- (1000 °C, 1s),[48] and Sr-doped HfO_2 films (800 °C, 20s).[49] Moreover, the FE capacitors with HfO_2-based films can work at high temperatures even up to 185 °C with the P_r larger than 8 μC cm^{-2}.[50,109] The remaining challenges include a lowering of the operation voltage as well as an increase in the endurance at least to the level of 10^{12}. Müller et al. recently reported the successful fabrication and electrical characterization of the three dimensional capacitors with Al-doped HfO_2 films. As seen in **Figure 8**a, 10 nm-thick Al-doped HfO_2 films were uniformly deposited on the Si trenches with an aspect ratio of 13:1. From Figure 8b, the P_r per projected area could be as large as 150 μC cm^{-2}, which is one order of magnitude larger than that of a planar capacitor.[47,50] La-doped HfO_2, the P_r of which is 45 μC cm^{-2}, could provide an even higher P_r per projected area.[50] It needs to be mentioned again that the most appropriate electrode material for the FE doped-HfO_2 layers is believed to be TiN, which can be deposited with a highly matured ALD process in mass production. In fact, many of the electrical properties on the FE doped-HfO_2 layers reported so far were already demonstrated in capacitors with ALD-TiN electrodes.[47] TiN is mechanically robust and cheap, employed as top and bottom electrodes for DRAM capacitors nowadays.[110] Therefore, an FE doped-HfO_2 layer is highly promising as the FE capacitor for a 1T–1C FeRAM.

4.1.2. Ferroelectric Field-Effect-Transistors

FeFET was first proposed in the late 1950s.[101] It was about 16 years later that the first silicon based FeFET was fabricated by Wu in 1974.[103] The structure of FeFET is quite simple. The gate oxide of the MOSFET is replaced by a FE layer, and the inversion/depletion or accumulation/depletion of carriers in semiconducting channel is modulated by the polarity of the FE polarization.[103] Therefore, the polarization switching of the FE will induce a threshold voltage (V_T) shift of the transistor. The resulting memory window (MW) can be estimated by MW ≈ $2E_C t_f$.

As a consequence, a reasonable memory window of the threshold voltage will call for either a very thick film or a rather high E_c. For traditional FEs like PZT or SBT, the E_c is in the range of 50–100 kV cm^{-1}, which implies that a t_f of at least 100 nm is necessary to achieve a memory window in the range of several volts.[111] However, the much higher E_c of
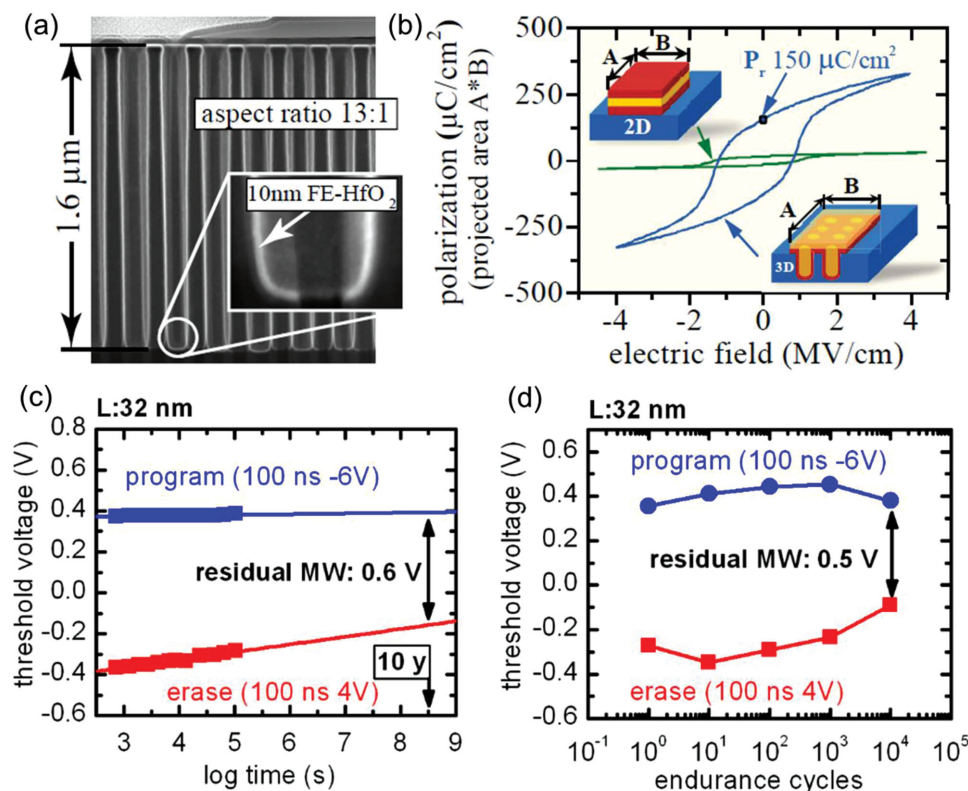
Figure 8. a) The cross sectional image of three dimensional capacitors with Si-doped HfO_2 capacitive layer analyzed using scanning transmission electron microscopy. b) The polarization–electric field curves of Si-doped HfO_2 capacitors with planar and three-dimensional structures. Panels (a,b) reproduced with permission.[50] Copyright 2014, IEEE. c) The retention and d) endurance characteristics of FeFET with 10 nm-thick Si-doped HfO_2 gate insulator. Panels (c,d) reproduced with permission.[113] Copyright 2014, IEEE.

doped HfO_2 allows scaling to the 10 nm range or even smaller, while still maintaining the reasonable memory window. For many years it has been quite difficult to achieve non-volatile retention in a FeFET. The reason is that in a metal–ferroelectric–semiconductor (MFS) system, the semiconductor works as one of the electrodes that causes a voltage drop across the whole structure. Moreover, when using traditional FEs, an interface layer has to be introduced, making a metal–ferroelectric–insulator–semiconductor (MFIS) structure, in order to avoid any undesirable interface reactions, including unwanted silicidation and SiO_2 formation. The non-FE interface layer will give rise to an additional voltage drop. Both effects lead to a depolarization field across the FE in the retention test.[112] With SBT as the FE, it was possible to achieve non-volatile retention by using a high-k dielectric ($HfSiO_x$) as the interface layer and making the FE rather thick.[112] J. Müller and Yurchuk et al., however, already reported that the FeFET fabricated using the Si-doped HfO_2 layer as the FE layer can be even scaled down to 28 nm with the robust retention properties as shown in Figure 8c.[113,114] They also reported that the FeFET could be operated with a very short pulse time of 20 ns, which is several orders of magnitude smaller than the standard floating gate flash memory cell. The memory window between the programmed and erased states decreased slightly after 10^5 seconds, but an extrapolated memory window of >600 mV was retained after 10 years.[113,114] As seen in Figure 8d, however, the endurance property was limited to 10^4 cycles at this stage. This can be

improved by engineering the stacks and the operating conditions.[115] In fact, with very high density of bits, the endurance of 10^4 could be sufficient for many applications.[110] Martin, S. Müller, J. Müller, and Yurchuk et al. reportedsimilar endurance and retention properties of the FeFET with Si-doped HfO_2 FE gate oxide.[109,114,116,117] Cheng et al. recently reported the FeFET with $Hf_{0.5}Zr_{0.5}O_2$ as the FE layer.[103] In their report, the FeFET could operate with a short pulse of 5 ns, and endure up to 10^{12} cycles with almost no decrease in the ratio of the current for programmed and erased states.[118] However, the selected voltage was rather low compared with the t_f, making the FE operate in a sub-loop rather than in the saturated states. As a consequence, the two memory states rapidly degraded during retention testing, and the retention time was in the 10^3 seconds range.[118] They reported that this FeFET can be used as a single transistor DRAM, for which retention time of a few tens of seconds is not a problem.[118] For the replacement of DRAM, however, they used too thick layer stacks, and as a consequence, a rather high operating voltage was necessary. Appropriate vertical scaling of this approach still has to be confirmed.

In summary, FE HfO_2 promises to solve the most severe issues of FeFET by its high E_c and thickness scalability. Studies of FeFET using HfO_2-based FE layers for the past few years have shown some impressive results and significant improvements in device fabrication and performance, making this approach a viable candidate for the next generation memories. FE HfO_2,

therefore, is expected to bring hope toward the scaling of the classical 1T–1C FeRAM and FeFET.

4.2. Non-Memory Applications using Antiferroelectric Films

4.2.1. Fundamentals for the Applications of AFE Films

The development of new technologies to harvest, store or manage energy is one of the most important issues in a modern society with exponentially increasing number of mobile electric devices.[7,51] Polar materials could be feasible candidates for such energy-related applications considering their large correlation coefficient with the P, E, S (entropy) and T (temperature).[53] Among them, AFE materials could be an even more interesting approach due to the lack of P at E = 0, while a very high change in P can be induced by an application of E or changing T. **Figure 9**a shows a schematic diagram of the thermodynamically reversible interactions that may occur among the thermal and electrical variables of polarizable materials.[53] First, the AFE films can work as dielectric materials which can store a large

charge or electric energy.[51] In fact, pure (non-hysteretic) HfO_2 or ZrO_2 films have been used as a high charge capacitive layer in MOSFET and DRAM, but the AFE HfO_2-based films might not be appropriate for this application due to the large hysteretic loss.[119] In contrast, the large magnitude of the electric field for FE-to-AFE phase transition, large maximum polarization, and small P_r of the AFE HfO_2-based films are appropriate for electrostatic energy storage applications.[51] Figure 9b shows the P–E hysteresis curve that explains the energy storage behavior of AFE materials.[51] The blue area refers to the recoverable part of the stored energy, which is called an energy storage density (ESD), and the green area refers to the unrecoverable loss due to the polarization switching. The pyroelectricity and ECE of the AFE HfO_2-based films that use the coupling of thermal and electrical properties can be used for various applications such as ECE, PEH, and IR sensors for thermal imaging.[53] In fact, the ECE is the physical inverse of the pyroelectricity. The ECE generally uses an isothermal entropy change (ΔS) and/or adiabatic temperature change (ΔT) from the poling/depoling of polar materials by applying/withdrawing an electric field to them.[5,6] For the actual cooling, various thermal cycles such
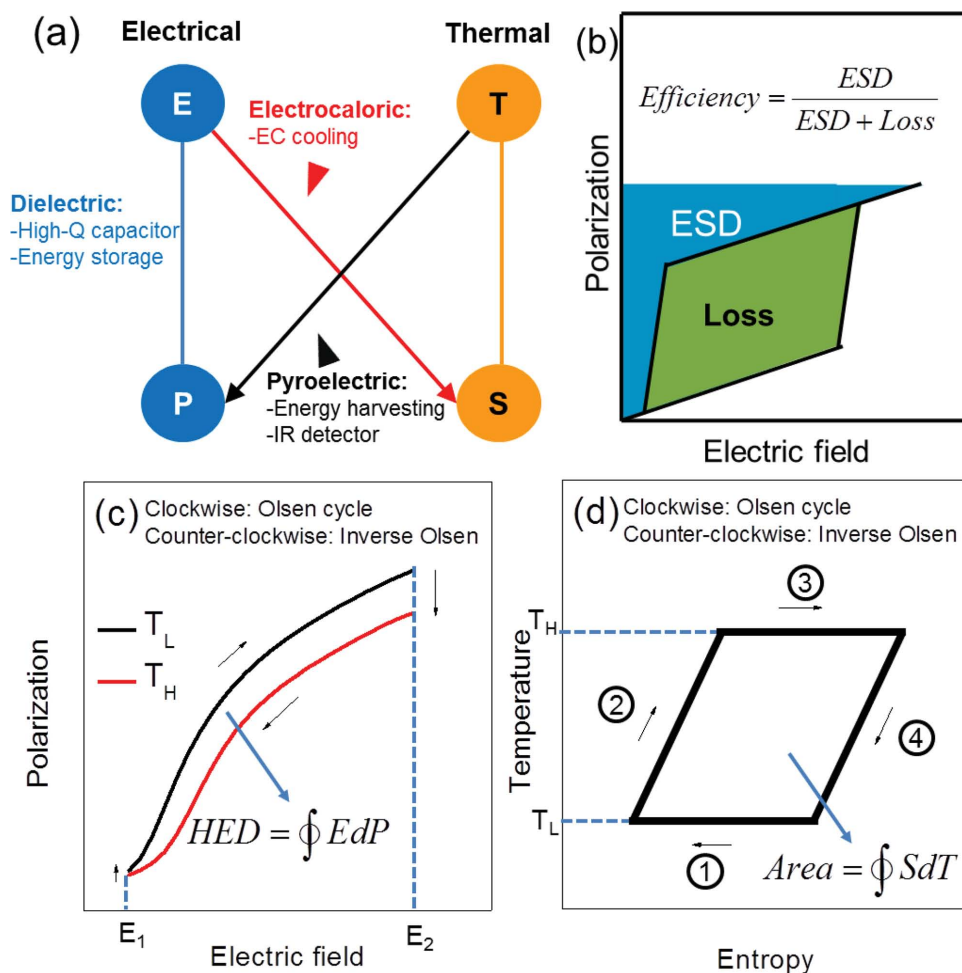

Figure 9. a) Schematic diagram showing the coupling of the electrical and thermal properties. Adapted with permission.[53] Copyright 2014, Elsevier. b) The schematic diagram for the calculation of energy storage density and loss from polarization–electric field hysteresis. Reproduced with permission.[51] c) Schematic diagrams showing the Olsen cycle for energy harvesting and electrocaloric cooling in temperature-dependent polarization–electric field curves.

as the Carnot, Ericsson, and Olsen cycles can be used and the Olsen cycle is discussed in this report for the direct comparison of ECE to the PEH.[22,120] As seen in Figure 9c, the Olsen cycle for ECE adopts the following steps (an anti-clockwise cycle): (1) poling of the pyroelectric material with an increasing electric field ($E_1 \to E_2$) at a low T (T_L), (2) partly depoling it by increasing T ($T_L \to T_H$), (3) depoling it by decreasing the electric field ($E_2 \to E_1$) at T_H, and (4) partly poling it by cooling it to the initial T_L. The degree of polarization of the polar materials is directly related to their entropy (S), so the poling/depoling of a pyroelectric material means extraction/absorption of the heat or entropy.[22,53,120] Figure 9d shows the schematic Olsen cycle for ECE in the T–S diagram.[53] In this case, the pyroelectric material releases the entropy at high temperature (T_H) and absorbs it at low temperature (T_L).[53] Since the magnitude of heat in an isothermal reversible process can be calculated from the product of the ΔS and T, the released heat ($T_H \Delta S$) is larger than the absorbed heat ($T_L \Delta S$) in the case of the single Olsen cycle for ECE.[53] Meanwhile, the Olsen cycle can also be used for the PEH (the clockwise cycle in Figure 9c and d).[53] In the

Olsen cycle for PEH, the pyroelectric materials absorb heat at T_H and release it at T_L, so they can transform the absorbed heat into an electrical energy.

4.2.2. Electrostatic Supercapacitors

Figure 10a shows the variations in ESD values of $Hf_{1-x}Zr_xO_2$ films ($0.7 \leq x \leq 0.9$) as a function of a pulse height used for the P–E measurement. Surprisingly, the ESD values of the Zr-rich $Hf_{1-x}Zr_xO_2$ films were all higher than 30 J cm^{-3}, which indicates far better performance compared with the well-studied Pb- and Ba-based perovskite AFE materials or PVDF-based AFE polymers.[11,51] Until now, the energy storage performances of the AFE HfO_2-based films with dopants other than Zr have not been reported. However, the AFE Si- and Al-doped HfO_2 films are also expected to be used as electrostatic supercapacitors with large ESD values. Especially, the slimmer hysteresis of the AFE Si-doped HfO_2 film is expected to increase the efficiency of energy storage.
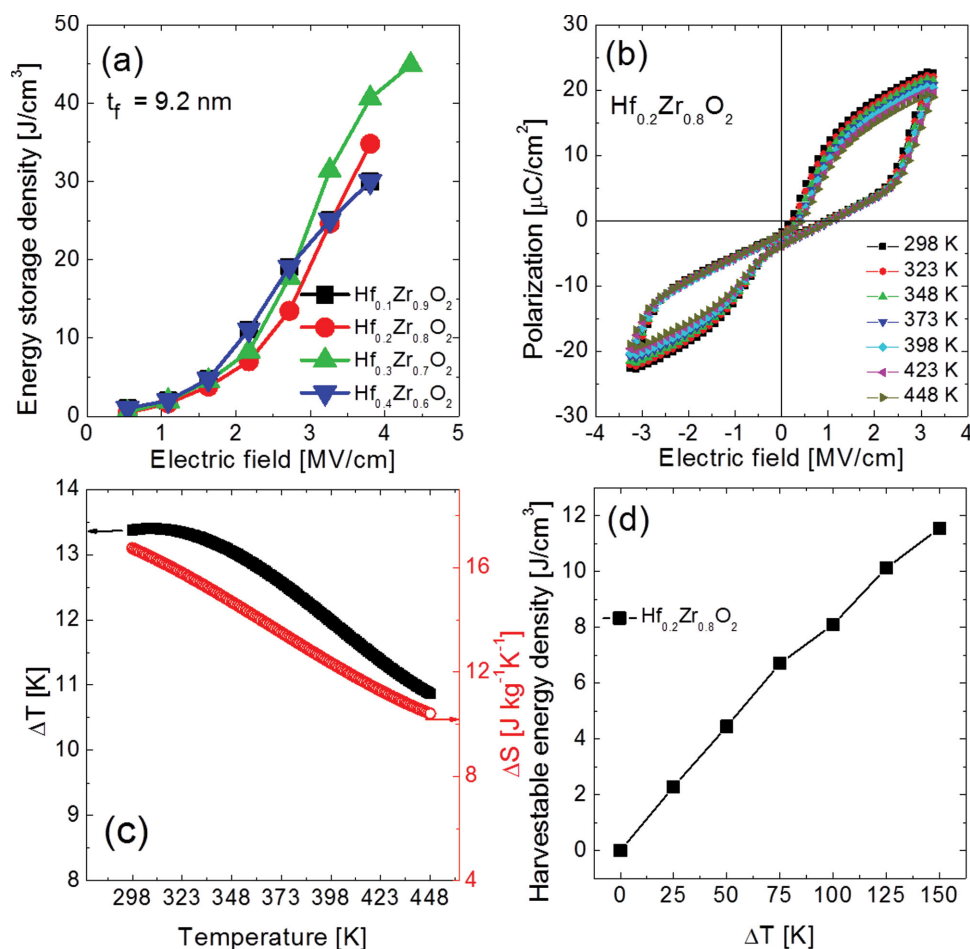

Figure 10. a) Variations in the energy storage densities of the $Hf_{1-x}Zr_xO_2$ films with various compositions (x = 0.6–0.9) as a function of the electric field. Reproduced with permission.[51] b) The polarization–electric field hysteresis curves of the ≈9.2 nm-thick $Hf_{0.2}Zr_{0.8}O_2$ thin film sandwiched by TiN top and bottom electrodes at various temperature of 298–448 K. Adapted with permission.[53] Copyright 2014, Elsevier. (Unpublished data.) c) The changes in ΔT (black solid dots) and ΔS (red open dots) as a function of temperature of the ≈9.2 nm-thick $Hf_{0.2}Zr_{0.8}O_2$ film. d) Change in the harvestable energy density calculated from the polarization–electric field curves of the ≈9.2 nm-thick $Hf_{0.2}Zr_{0.8}O_2$. The data in panels (c,d) are from ref. [53].

4.2.3. Electrocaloric Coolers

The development of new eco-friendly technologies for refrigeration or cooling is one of the most important issues of modern society. Especially, the development of a new solid-state-cooling technology is highly required due to the increase usage of electric devices with integrated computer chips. To solve this problem, ECE has been intensively studied since the report on the giant ECE of $PbZr_{0.95}Ti_{0.05}O_3$ films by Mischenko et al.[5] The cooling performance of an ECE material has been indirectly estimated by calculating the ΔT and ΔS based on the well-known Maxwell's relation of $(\partial S/\partial E)_T = (\partial P/\partial T)_E$. The magnitude of ΔT and ΔS can be calculated using Equation (1) and (2), respectively,[5,6]

$$\Delta T = -\frac{1}{\rho C}\int_{E_1}^{E_2} T\left(\frac{\partial P}{\partial T}\right)_E dE \qquad (1)$$

$$\Delta S = -\frac{1}{\rho}\int_{E_1}^{E_2}\left(\frac{\partial P}{\partial T}\right)_E dE \qquad (2)$$

where ρ and C are the density and specific heat, respectively.

Park et al. recently reported the ECE of 9.2 nm-thick $Hf_{0.2}Zr_{0.8}O_2$ films.[52] Figure 10c shows the polarization–electric field hysteresis curve of the $Hf_{0.2}Zr_{0.8}O_2$ film at the temperature range of 298–448 K.[52] The polarization values generally decreased, and the electric field for the AFE-to-FE and FE-to-AFE transition decreased with increasing temperature.[52] For the whole temperature range of the measurements, however, the electric field-induced phase transition could be clearly observed.[52] Figure 10c shows the change in ΔT and ΔS as a function of temperature,[52] and the large ΔT (10.9–13.4 K)

and ΔS (10.7–16.7 J kg^{-1} K^{-1}) values in a wide temperature range of 298–448 K were confirmed.[53] For the conventional electrocaloric materials, on the other hand, such a large value of ΔT and ΔS could be observed only within a narrow temperature range near the Curie temperature.[5,6,23,121–124] The reason why $Hf_{0.2}Zr_{0.8}O_2$ films can have a large ΔT and ΔS has yet to be defined. However, it is believed that the stable field-induced phase transition in the wide temperature range might be directly related to it. There should be a large ΔS due to the phase transition, and the $(\partial P/\partial T)_E$ values were also the largest near the transition electric field.[21] The upper panel of **Table 2** summarizes the ECEs of various materials.[5,6,23,121–124] The paper by Park et al.[53] is a pioneering report on the ECE of the HfO$_2$-based AFEs, and it is believed that these materials could show even larger ΔT and ΔS by optimizing their film orientation, increasing the portion of the AFE phase, and applying different dopants to HfO$_2$ films. Especially, the AFE Si- or Al-doped films are also believed to show giant ECE with large ΔT and ΔS values.

4.2.4. Pyroelectric Energy Harvesters

Large amounts of waste heat generated is a serious problem today.[125] Especially, computers are contributing an ever growing portion among the various sources of waste heat. Therefore, the conversion of the wasted heat from high-speed computers into electrical energy could have a huge impact. The PEH is one of the promising methods for this energy conversion due to its high potential efficiency.[126] Among the various mechanisms for the PEH, Sebald et al. reported that the Olsen cycle was the most promising method with a large harvestable energy density (HED) per single cycle.[120] HED refers to the

Table 2. The electrocaloric effect (upper panel) and pyroelectric energy harvesting properties (bottom panel) of various materials. Data from ref. [53] and references therein.

	Material	T [K]	ΔT [K]	ΔE [kV cm^{-1}]	ΔT/ΔE [K cm kV^{-1}]	ΔS [J K^{-1}kg^{-1}]
Lead-containing	$PbZr_{0.95}Ti_{0.05}O_3$[5]	495	12	481	0.025	8
	$Pb_{0.8}Ba_{0.2}ZrO_3$[121]	290	45.3	598	0.076	46.9
	$PbSc_{0.5}Ta_{0.5}O_3$[122]	341	6.2	774	0.008	6.3
	$0.9PbMg_{1/3}Nb_{2/3}O_3$–$0.1PbTiO_3$[123]	348	5	895	0.006	5.6
	P(0.55VDF-0.45TrFE)[6,23]	353	12.6	2090	0.006	60
Lead-free	$SrBi_{2.1}Ta_2O_9$[124]	500	4.9	600	0.008	N/A
	$Hf_{0.2}Zr_{0.8}O_2$[53]	298	13.4	3260	0.004	16.7
	Material	Form	HED [J cm^{-3} cycle^{-1}]	E [kV cm^{-1}]	T$_{HL}$ [K]	Method
Lead-containing	$0.90PbMg_{1/3}Nb_{2/3}O_3$–$0.10PbTiO_3$[22]	Ceramic	0.186	35	50	Direct
	$0.68PbMg_{1/3}Nb_{2/3}O_3$–$0.32PbTiO_3$[130]	Single crystal	0.100	7	90	Direct
	$(Pb,La)(Zr_{0.65}Ti_{0.35})O_3$[131]	Ceramic	1.014	68	170	Direct
Lead-free	P(VDF-TrFE)[129]	Thin film	0.521	300	85	Direct
	P(VDF-TrFE)[128]	Thin film	0.155	150	85	Direct
	$(Bi_{0.5}Na_{0.5})_{0.915}$-$(Bi_{0.5}K_{0.5})_{0.05}Ba_{0.02}Sr_{0.015}TiO_3$[127]	Ceramic	1.523	39	140	Indirect
	$Hf_{0.2}Zr_{0.8}O_2$[53]	Thin film	11.549	3260	150	Indirect

internal area of the Olsen cycle in Figure 10b.[53] The details of the Olsen cycle were presented in the previous section, and it should be noted that the PEH is the inverse cycle of ECE. There have been many reports to harvest energy from waste heat via the Olsen cycle. The conditions needed for efficient and eco-friendly PEH could be summarized as follows: (1) a large HED, (2) a lead-free composition, (3) a thin film or nanostructure form, (4) stability against the T fluctuation, and (5) high electrical breakdown strength.[53]

Figure 10d shows the change in HED of the $Hf_{0.2}Zr_{0.8}O_2$ film as a function of temperature span used in the Olsen cycle.[53] The HED of the $Hf_{0.2}Zr_{0.8}O_2$ film was the largest among the films with various compositions, and its HED values were 2.3, 4.4, 6.7, 8.1, 10.1, and 11.5 J cm^{-3} for the temperature spans of 25, 50, 75, 100, 125, and 150 K, respectively. The maximum HED value of the $Hf_{0.2}Zr_{0.8}O_2$ film is ≈7.6 times larger than the largest HED value ever reported from other materials.[22,126–131] The bottom panel of Table 2 summarizes the PEH performances of various materials using the Olsen cycle.[22,126–131] Until now, only the PEH properties of $Hf_{1-x}Zr_xO_2$ films have been examined, but it is believed that the AFE HfO_2 based films with other dopants would be also promising for PEH.

4.2.5. IR Sensor for Thermal Imaging

Pyroelectric materials can be used as IR sensors for thermal imaging.[8,24,132] The array-based IR sensors can be used for people counting, health care, security, thermal imaging, and military application.[24] For these applications, the development of low-cost materials with high figure of merit is required. To achieve low-cost IR sensors, materials which are compatible for the templates commonly used in industry, such as Si substrates, are preferred.[8,24] Therefore, the AFE HfO_2-based films can be a promising candidate for this application, with its Si-compatibility. For the IR sensor application, the figure of merit is $F_v = p/C\varepsilon_r\varepsilon_0$, where p, T, C, ε_r, and ε_0 are the pyroelectric coefficient, operation temperature, heat capacity, dielectric permittivity, and permittivity of vacuum, respectively.[132] The most promising candidates for this application are thought to be $LiNbO_3$ and $LiTaO_3$ due to their moderate p and low ε_r; the F_v values of $LiNbO_3$ and $LiTaO_3$ are 10.8×10^{-2} and 11.6×10^{-2} m^2 C^{-1}, respectively.[132] The calculated F_v of the $Hf_{0.2}Zr_{0.8}O_2$ film was 32.0×10^{-2} m^2 C^{-1}, which is 2.8 times larger than that of $LiTaO_3$.

To summarize the energy related applications of AFE materials, the large HED, ΔT (or ΔS), ESD, k^2, and F_v values of the AFE $Hf_{1-x}Zr_xO_2$ films show that they are promising candidates for the next-generation nanoscale energy harvesting, electrocaloric cooling, electrostatic energy storage (EES), and thermal imaging systems.[53] Moreover, their lead-free, thermally stable, and highly Si-compatible nature, combined with the mature deposition techniques makes them even more attractive for mass-production. Notably, the PEH, ECE, EES, and IR sensing performances of the $Hf_{1-x}Zr_xO_2$ films in this and previous studies are still in the pioneering stage, and could be improved further with various strategies, such as control of the film orientation, suppression of the formation of the second phase, and adoption of various dopants. Moreover, they can be integrated

in a single Si wafer, which is the most industry-friendly template for mass production, and can be used as a monolithic device.

5. Conclusions

In conclusion, the recent progresses on the FE and AFE properties of HfO_2-based thin films since 2011 have been comprehensively reviewed. It is believed that the origin of the unexpected FE property is the formation of the polar oIII-phase, which cannot be observed in the general phase diagram of HfO_2. Based on various computational calculations and experimental works, there are many conditions to be met for the formation of the oIII-phase: small D_{ave} to prevent the formation of the m-phase and to stabilize the metastable t-phase, a large tensile stress along the c-axis of the t-phase, and an upper capping layer to prevent the formation of the m-phase during crystallization annealing. Appropriate orientation of the t-phase grains before the phase transition to oIII-phase must be compatible with the asymmetric strain and polar direction. The various dopants, such as Si, Zr, Y, Al, Gd, Sr, and La, can stabilize the oIII-phase with appropriate doping concentrations, which may alter the surface energy (so that the transition to the metastable t- or oIII-phase can be formed.), and internal stress state. The films could be deposited via various deposition techniques, such as ALD, sputtering, and CSD. The FE HfO_2-based films can be used for the FE capacitive layer of FeRAM and FE gate oxide materials of FeFET. It is believed that FE doped HfO_2 films can drive the technology node of the state-of-the-art FeRAM from >100 nm to ≈20 nm, due to its mature ALD technique and small t_f. Furthermore, TiN, which is currently used as an electrode material for state-of-the-art DRAM, can be used as an electrode material for the doped HfO_2-based films. For applications of the FeFET, due to the large E_c (≈1 MV cm^{-1} level) of doped HfO_2-based films, a reasonable memory window can be achieved, as the difference between the threshold voltages of the two polarization states can be large for an extremely small thickness of ≈10 nm. Moreover, the retention time for the sufficient memory window between the programmed and erased states was impressive, but it needs to be improved further to meet the general 10 year criterion, which could be solved by a better interface and process control. With optimization of the fabrication process, impressive endurance (10^{10} cycles) could be observed in the FeFET structure. However, if this device is considered to be the successor of DRAM, its endurance must be significantly improved. Nevertheless, the impressive performance, easy fabrication by ALD, and small t_f (<10 nm) of the HfO_2-based FE films could invoke renewed interest in the field of FE memories. AFE HfO_2-based films seem to be promising for various applications, such as electrostatic supercapacitors, electrocaloric cooler, pyroelectric energy harvester, and IR sensor for thermal imaging. Their performances calculated from the double hysteretic P–E curves over a wide temperature range provided promising aspects that the HfO_2-based (more precisely ZrO_2-based) AFE films could overwhelm the performances of the conventional materials which are too thick, difficult to make, and even not environmentally friendly. These aspects show that the new AFE materials could be the material

of choice for the monolithic integration of computer chips with various passive components, with energy saving, energy harvesting and imaging functionalities in environmentally benign manner.

Supporting Information

Supporting Information is available from the Wiley Online Library or from the author.

Acknowledgements

[1] J. Valasek, *Phys. Rev.* **1920**, *15*, 527.

[2] J. Valasek, *Phys. Rev.* **1921**, *17*, 475.

[3] M. E. Lines, A. M. Glass, *Principles and Applications of Ferroelectrics and Related Materials*, Oxford University Press, Oxford, UK **2001**.

[4] J. F. Scott, *Ferroelectric Memories*, Springer-Verlag, Berlin, Germany **2000**.

[5] A. S. Mischenko, Q. Zhang, J. F. Scott, R. W. Whatmore, N. D. Mathur, *Science* **2006**, *311*, 1270.

[6] B. Neese, B. Chu, S.-G. Lu, Y. Wang, E. Furman, Q. M. Zhang, *Science* **2008**, *321*, 821.

[7] C. R. Bowen, H. A. Kim, P. M. Weaver, S. Dunn, *Energy Environ. Sci.* **2014**, *7*, 25.

[8] R. W. Whatmore, *J. Electroceram*. **2004**, *13*, 139.

[9] C. Dubourdieu, J. Bruley, T. Arruda, A. Posadas, J. Jordan-Sweet, M. Frank, E. Cartier, D. Frank, S. Kalinin, A. Demkov, V. Narayanan, *Nat. Nanotechnol.* **2013**, *8*, 748.

[10] M. Takahashi, S. Sakai, *Jpn. J. Appl. Phys.* **2005**, *44*, L800.

[11] K. Kim, Y. J. Song, *Microelectron. Reliab.* **2003**, *43*, 385.

[12] D. S. Jeong, R. Thomas, R. S. Katiyar, J. F. Scott, H. Kohlstedt, A. Petraru, C. S. Hwang, *Rep. Prog. Phys.* **2012**, *75*, 076502.

[13] N. Setter, D. Damjanovic, L. Eng, G. Fox, S. Gevorgian, S. Hong, A. Kingon, H. Kohlstedt, N. Y. Park, G. B. Stephenson, I. Stolitchnov, A. K. Tagantsev, D. V. Taylor, T. Yamada, S. Streiffer, *J. Appl. Phys.* **2006**, *100*, 051606.

[14] L. D. Landau, *Phys. Z. Sowjet* **1937**, *11*, 26.

[15] A. F. Devonshire, *Phil. Mag.* **1949**, *40*, 1040.

[16] V. L. Ginzburg, L. D. Landau, *Zh. Exp. Theor. Fiz.* **1950**, *20*, 1064.

[17] C. Kittel, *Phys. Rev.* **1951**, *82*, 729.

[18] X. Hao, J. Zhai, L. B. Kong, Z. Xu, *Prog. Mater. Sci.* **2014**, *63*, 1.

[19] K. Yao, S. Chen, M. Rahimabady, M. S. Mirshekarloo, S. Yu, F. E. H. Tay, T. Sritharan, L. Lu, *IEEE T. Ultrason. Ferr.* **2011**, *58*, 1968.

[20] J. Li, S. Tan, S. Ding, H. Li, L. Yang, Z. Zhang, *J. Mater. Chem.* **2012**, *22*, 23468.

[21] S. E. Reyes-Lillo, K. F. Garrity, K. M. Rabe, arXiv:cond-mat/1403.3878, **2014**.

[22] G. Sebald, S. Pruvost, D. Guyomar, *Smart Mater. Struct.* **2008**, *17*, 015012.

[23] S.-G. Lu, Q. Zhang, *Adv. Mater.* **2009**, *21*, 1983.

[24] A. J. Holden, *IEEE T. Ultrason. Ferr.* **2011**, *58*, 1981.

[25] E. Bersch, S. Rangan, R. A. Bartynsku, E. Garfunkel, E. Vescovo, *Phys. Rev. B* **2008**, *78*, 085114.

[26] S. Desgreniers, K. Lagarec, *Phys. Rev. B* **1999**, *59*, 8467.

[27] R. Thielsch, A. Gatto, J. Heber, N. Kaiser, *Thin Solid Films* **2002**, *410*, 86.

[28] V. George, S. Jahagirdar, C. Tong, K. Smits, S. Damaraju, S. Siers, V. Naydenov, T. Khondker, S. Sarkar, P. Singh, in *Proc. IEEE Asian Solid-State Circuits Conf.* **2007**, 14.

[29] T. S. Böscke, J. Müller, D. Bräuhaus, U. Schröder, U. Böttger, *Appl. Phys. Lett.* **2011**, *99*, 102903.

[30] U. Schroeder, E. Yurchuk, J. Müller, D. Martin, T. Schenk, P. Polakowski, C. Adelmann, M. I. Popovici, S. V. Kalinin, T. Mikolajick, *Jpn. J. Appl. Phys.* **2014**, *53*, 08LE02.

[31] T. S. Böscke, St. Teichert, D. Bräuhaus, J. Müller, U. Schröder, U. Böttger, T. Mikolajick, *Appl. Phys. Lett.* **2011**, *99*, 112904.

[32] D. Zhou, J. Müller, J. Xu, S. Knebel, D. Bräuhaus, U. Schröder, *Appl. Phys. Lett.* **2012**, *100*, 082905.

[33] D. Zhou, J. Xu, Q. Lu, Y. Guan, F. Cao, X. Dong, J. Müller, T. Schenk, U. Schröder, *Appl. Phys. Lett.* **2013**, *103*, 192904.

[34] E. Yurchuk, J. Müller, S. Knebel, J. Sundqvist, A. P. Graham, T. Melde, U. Schröder, T. Mikolajick, *Thin Solid Films* **2013**, *533*, 88.

[35] P. D. Lomenzo, P. Zhao, Q. Takmeel, S. Moghaddam, T. Nishida, M. Nelson, C. M. Fancher, E. D. Grimley, X. Sang, J. M. LeBeau, J. L. Jones, *J. Vac. Sci. Technol. B* **2014**, *32*, 03D123.

[36] J. Müller, T. S. Böscke, D. Bräuhaus, U. Schröder, U. Böttger, J. Sundqvist, P. Kücher, T. Mikolajick, L. Frey, *Appl. Phys. Lett.* **2012**, *99*, 112901.

[37] J. Müller, T. S. Böscke, U. Schröder, S. Mueller, D. Bräuhaus, U. Böttger, L. Frey, T. Mikolajick, *Nano Lett.* **2012**, *12*, 4318.

[38] M. H. Park, H. J. Kim, Y. J. Kim, W. Lee, H. K. Kim, C. S. Hwang, *Appl. Phys. Lett.* **2013**, *102*, 112914.

[39] M. H. Park, H. J. Kim, Y. J. Kim, W. Lee, T. Moon, C. S. Hwang, *Appl. Phys. Lett.* **2013**, *102*, 242905.

[40] M. H. Park, H. J. Kim, Y. J. Kim, T. Moon, C. S. Hwang, *Appl. Phys. Lett.* **2014**, *104*, 072901.

[41] M. H. Park, H. J. Kim, Y. J. Kim, W. Jeon, T. Moon, C. S. Hwang, *Phys. Status Solidi RRL* **2014**, *8*, 532.

[42] M. H. Park, H. J. Kim, Y. J. Kim, W. Lee, T. Moon, K. D. Kim, C. S. Hwang, *Appl. Phys. Lett.* **2014**, *105*, 072902.

[43] J. Müller, U. Schröder, T. S. Böscke, I. Müller, U. Böttger, L. Wilde, J. Sundqvist, M. Lemberger, P. Kücher, T. Mikolajick, L. Frey, *J. Appl. Phys.* **2011**, *110*, 114113.

[44] T. Olsen, U. Schröder, S. Müller, A. Krause, D. Martin, A. Singh, J. Müller, M. Geidel, T. Mikolajick, *Appl. Phys. Lett.* **2012**, *101*, 082905.

[45] S. Starschich, D. Griesche, T. Schneller, R. Waser, U. Böttger, *Appl. Phys. Lett.* **2014**, *104*, 202903.

[46] S. Mueller, J. Mueller, A. Singh, S. Riedel, J. Sundqvist, U. Schroeder, T. Mikolajick, *Adv. Funct. Mater.* **2012**, *22*, 2412.

[47] P. Polakowski, S. Riedel, W. Weinreich, M. Rudolf, J. Sundqvist, K. Seidel, J. Müller, in *Proc. IEEE 6th International Memory Workshop* **2014**, 1.

[48] S. Mueller, C. Adelmann, A. Singh, S. V. Elshocht, U. Schroeder, T. Mikolajick, *ECS J. Solid St. Sci.* **2012**, *1*, N123.

[49] T. Schenk, S. Mueller, U. Schroeder, R. Materlik, A. Kersch, M. Popovici, C. Adelmann, S. V. Elshocht, T. Mikolajick, in *Proc. Eur. Solid-State Device Res.Conf.* **2013**, 260.

[50] J. Müller, T. S. Böscke, Y. Yurchuk, P. Polakowski, J. Paul, D. Martin, T. Schenk, K. Khullar, A. Kersch, W. Weinreich, S. Riedel, K. Seidel, A. Kumar, T. M. Arruda, S. V. Kalinin, T. Schlosser, R. Boschke, R. van Bentum, U. Schröder, T. Mikolajick, in *IEEE International Electron Devices Meeting 2013*, 10.8.1.

[51] M. H. Park, H. J. Kim, Y. J. Kim, T. Moon, K. D. Kim, C. S. Hwang, *Adv. Energy Mater.* **2014**, *4*, 1400610.

[52] M. H. Park, H. J. Kim, Y. J. Kim, W. Lee, T. Moon, K. D. Kim, C. S. Hwang, unpublished.

[53] M. H. Park, H. J. Kim, Y. J. Kim, T. Moon, K. D. Kim, C. S. Hwang, *Nano Energy* **2015**, *12*, 131.

[54] M. H. Park, H. J. Kim, Y. J. Kim, T. Moon, K. D. Kim, C. S. Hwang, *Phys. Status Solidi RRL* **2014**, *8*, 857.

[55] G. H. Kim, H. J. Lee, A. Q. Jiang, M. H. Park, C. S. Hwang, *J. Appl. Phys.* **2009**, *105*, 044106.

[56] H. J. Lee, G. H. Kim, M. H. Park, A.-Q. Jiang, C. S. Hwang, *Appl. Phys. Lett.* **2010**, *96*, 212902.

[57] M. H. Park, H. J. Lee, G. H. Kim, Y. J. Kim, J. H. Kim, J. H. Lee, C. S. Hwang, *Adv. Funct. Mater.* **2011**, *21*, 4305.

[58] A. Q. Jiang, H. J. Lee, G. H. Kim, C. S. Hwang, *Adv. Mater.* **2009**, *21*, 2870.

[59] A. E. Feuersanger, in *Thin film dielectrics* (Ed: F. Vratny), *Electrochemical Society Inc.*, New York **1969**.

[60] C. S. Hwang, *Atomic Layer Deposition for Semiconductors*, Springer, New York, USA **2013**.

[61] O. Ohtaka, H. Fukui, T. Kunisada, T. Fujisawa, K. Funakoshi, W. Utsumi, T. Irifune, K. Kuroda, T. Kikegawa, *J. Am. Ceram. Soc.* **2001**, *84*, 1369.

[62] T. D. Huan, V. Sharma, G. A. Rossetti Jr., R. Ramprasad, arXiv:cond-mat/1407.1008, **2014**.

[63] J. E. Lowther, J. K. Dewhurst, J. M. Leger, J. Haines, *Phys. Rev. B* **1999**, *60*, 14485.

[64] C. J. Howard, E. H. Kisi, O. Ohtaka, *J. Am. Ceram. Soc.* **1991**, *74*, 2321.

[65] E. H. Kisi, *J. Am. Ceram. Soc.* **1998**, *81*, 741.

[66] H. Arashi, *J. Am. Ceram. Soc.* **1992**, *75*, 844.

[67] E. H. Kisi, C. J. Howard, E. H. Kisi, *Key Eng. Mat.* **1998**, *153*, 1.

[68] S. Clima, D. J. Wouters, C. Adelman, T. Schenk, U. Schroeder, M. Jurczak, G. Pourtois, *Appl. Phys. Lett.* **2014**, *104*, 092906.

[69] R. Materlik, A. Kersch, Ch. Künneth, unpublished.

[70] M. Kohli, P. Muralt, N. Setter, *Appl. Phys. Lett.* **1998**, *72*, 3217.

[71] C. Richter, T. Schenk, U. Schroeder, T. Mikolajick, presented at Baltic ALD Conf., Helsinki, Finland, May, **2014**.

[72] M. Hoffmann, T. Schenk, I. Kulemanov, C. Adelmann, M. Popovici, U. Schroeder, T. Mikolajick, unpublished.

[73] R. C. Garvie, *J. Phys. Chem.* **1965**, *69*, 1238.

[74] R. C. Garvie, *J. Phys. Chem.* **1978**, *82*, 218.

[75] M. W. Pitcher, S. V. Ushakov, A. Navrotsky, B. F. Woodfield, G. Li, J. Boerio-Goates, *J. Am. Ceram. Soc.* **2005**, *88*, 160.

[76] M. Shandalov, P. C. McIntyre, *J. Appl. Phys.* **2009**, *106*, 084322.

[77] D.-Y. Cho, H. S. Jung, I. -H. Yu, J. H. Yoon H. K. Kim, S. Y. Lee, S. H. Jeon, S. W. Han, J. H. Kim, T. J. Park, B.-G. Park, C. S. Hwang, *Chem. Mater.* **2012**, *24*, 3534.

[78] S. K. Kim, C. S. Hwang, *Electrochem. Solid St.* **2008**, *11*, G9.

[79] A. Gruverman, O. Kolosov, J. Hatano, K. Takahashi, H. Tokumoto, *J. Vac. Sci. Technol. B* **1995**, *13*, 1095.

[80] M. V. Nevitt, Y. Fang, S. K. Chan, *J. Am. Ceram. Soc.* **1990**, *73*, 2502.

[81] T. Tojo, T. Atake, T. Mori, H. Yamamura, *J. Chem. Thermodyn.* **1999**, *31*, 831.

[82] J. E. Jaffe, R. A. Bachorz, M. Gutowski, *Phys. Rev. B* **2005**, *72*, 144107.

[83] P. Simoncic A.Navrosky, *J. Mater. Res.* **2007** *22*, 876.

[84] W. D. Nix, B. M. Clemens, *J. Mater. Res.* **1999**, *14*, 3467.

[85] M. H. Park, *Ph.D thesis*, Seoul National University (Seoul, Korea), Feb., **2014**.

[86] M. Hoffmann, U. Schroeder, T. Schenk, C. Adelmann, M. Popovici, T. Mikolajick, unpublished.

[87] J. F. Scott, M. Dawber, *Appl. Phys. Lett.* **2000**, *76*, 3801.

[88] I. K. Yoo, S. B. Desu, *Phys. Status Solidi A* **1992**, *133*, 565.

[89] C.-K. Lee, E. Cho, H.-S. Lee, C. S. Hwang, S. Han, *Phys. Rev. B* **2008**, *78*, 012102.

[90] U. Schroeder, S. Mueller, J. Mueller, E. Yurchuk, D. Martin, C. Adelmann, T. Schloesser, R. van Bentum, T. Mikolajick, *ECS J. Solid St. Sci.* **2013**, *2*, N69.

[91] J. C. Slater, *J. Chem. Phys.* **1964**, *41*, 3199.

[92] L. Zhao, M. Nelson, H. Aldridge, T. Iamsasri, C. M. Fancher, J. S. Forrester, S. Nishida, S. Moghaddam, J. L. Jones, *J. Appl. Phys.* **2014**, *115*, 034104.

[93] J. A. Speer, B. J. Cooper, *Am. Mineral.* **1982**, *67*, 804.

[94] D. Martin, J. Mueller, T. Schenk, T. M. Arruda, A. Kumar, E. Strelcov, E. Yurchuk, S. Mueller, D. Pohl, U. Schroeder, S. V. Kalinin, T. Mikolajick, *Adv. Mater.* **2014**, *26*, 8198.

[95] P. D. Lomenzo, Q. Takmeel, C. Zhou, Y. Liu, C. M. Fancher, J. L. Jones, S. Moghaddam, T. Nishida, *Appl. Phys. Lett.* **2014**, *105*, 072906.

[96] S. Mueller, J. Müller, U. Schroeder, T. Mikolajick, *IEEE Trans. Device Mater. Reliab.* **2013**, *13*, 93.

[97] T. Shimizu, T. Yokouchi, T. Shiraishi, T. Oikawa, P. S. S. R. Krishnan, H. Funakubo, *Jpn. J. Appl. Phys.* **2014**, *53*, 09PA04.

[98] D. A. Buck, *Master's thesis*, Massachusetts Institute of Technology (Cambridge, MA, USA) **1952**.

[99] J. R. Anderson, *Trans. Amer. Inst. Elect. Engrs.* **1953**, *71*, 395.

[100] J. Merz, J. R. Anderson, *Bell Lab Records* **1955**, *33*, 335.

[101] a) D. H. Looney, US patent no. 2791758, 1957; b) W. L. Brown, US patent no. 2791759, 1957; c) I. M. Ross, US patent no. 2791760 1957; d) J. A. Morton, US patent no. 2791761, 1957.

[102] D. Bondurant, *Ferroelectrics* **1990**, *112*, 273.

[103] S. Y. Wu, *IEEE Trans. Electron. Devices* **1974**, *21*, 499.

[104] H. P. McAdams, R. Acklin, T. Blake, X.-H. Du, J. Eliason, J. Fong, W. F. Kraus, D. Liu, S. Madan, T. Moise, S. Natarajan, N. Qian, Y. Qiu, K. A. Remack, J. Rodriguez, J. Roscher, A. Seshadri, S. R. Summerfelt, *IEEE J. Solid-St. Circ.* **2004**, *39*, 667.

[105] J.-M. Koo, B.-S. Seo, S. Kim, S. Shin, J.-H. Lee, H. Baik, J.-H. Lee, J. H. Lee, B.-J. Bae, J.-E. Lim, D.-C. Yoo, S.-O. Park, H.-S. Kim, H. Han, S. Baik, J.-Y. Choi, Y. J. Park, Y. Park, in *Electron Devices Meeting IEDM Tech. Digest.* **2005**, 340.

[106] S. Shin, J.-M. Koo, S. Kim, B.-S. Seo, J.-H. Lee, H. Baik, Y. Park, H. Han, S. Baik, J. K. Lee, *J. Nanosci. Nanotechnol.* **2006**, *6*, 3333.

[107] C.-U. Pinnow, T. Mikolajick, *J. Electrochem. Soc.* **2004**, *151*, K13.

[108] W. Hartner, P. Bosk, G. Schindler, H. Bachhofer, M. Moert, H. Wendt, T. Mikolajick, C. Dehm, H. Schroeder, R. Waser, *Appl. Phys. A* **2003**, *77*, 571.

[109] S. Mueller, S. R. Summerfelt, J. Müller, U. Schroeder, T. Mikolajick, *IEEE Electron Device Lett.* **2012**, *33*, 1300.

[110] International Technology Roadmap for Semiconductor 2013 Edition,http://www.itrs.net/Links/2013ITRS/Home2013.htm, accessed: September, 2014.

[111] L. Van Hai, T. Mitsue, S. Shigeki, in *Proc. International Memory Workshop* **2011**, 1.

[112] T. P. Ma, J.-P. Han, *IEEE Electron Device Lett.* **2002**, *23*, 386.

[113] J. Müller, E. Yurchuk, J. Paul, R. Hoffmann, S. Müller, D. Martin, S. Slesazeck, P. Polakowski, J. Sundqvist, M. Czernohorsky, K. Seidel, P. Kücher, R. Boschke, M. Trentzsch, K. Gebauer, U. Schröder, T. Mikolajick, in *Symp. on VLSI Technology Digest of Technical Papers* **2012**, 25.

[114] E. Yurchuk, J. Müller, J. Paul, T. Schlösser, D. Martin, R. Hoffmann, S. Müller, S. Slesazeck, U. Schröder, R. Boschke, R. van Bentum, T. Mikolajick, *IEEE Trans. Electron Devices* **2014**, *61*, 3699.

[115] E. Yurchuk, J. Müller, J. Paul, R. Hoffmann, S. Müller, D. Martin, S. Slesazeck, U. Schröder, J. Sundqvist, T. Schlösser, R. Boschke, R. van Bentum, M. Trentzsch, T. Mikolajick, in *Proc. IEEE International Reliability Physics Symposium* **2014**, 2E.5.1.

[116] D. Martin, E. Yurchuk, S. Müller, J. Müller, J. Paul, J. Sundqvist, S. Slesazeck, T. Schlösser, R. van Bentum, M. Trentzsch, U. Schroeder, T. Mikolajick, *Solid-State Electronics* **2013**, *88*, 65.

[117] S. Mueller, J. Müller, R. Hoffmann, E. Yurchuk, T. Schlösser, R. Boschke, J. Paul, M. Goldbach, T. Herrmann, A. Zaka, U. Schröder, T. Mikolajick, *IEEE Trans. Electron Devices* **2013**, *60*, 4199.

[118] C.-H. Cheng, A. Chin, *IEEE Electron Device Lett.* **2014**, *35*, 1.

[119] M. Mackaym, D. E. Schuele, L. Zhu, L. Flandinm M. A. Wolak, J. S. Shirk, A. Hiltner, E. Baer, *Macromolecules* **2012**, *45*, 1954.

[120] G. Sebald, E. Lefeuvre, D. Guyomar, *IEEE Trans. Ultrason. Ferroelectr. Freq. Control.* **2008**, *55*, 538.

[121] B. Peng, H. Fan, Q. Zhang, *Adv. Funct. Mater.* **2013**, *23*, 2987.

[122] T. M. Correia, S. Kar-Narayan, J. S. Young, J. F. Scott, N. D. Mathur, R. W. Whatmore, Q. Zhang, *J. Phys. D: Appl. Phys.* **2011**, *44*, 165407.

[123] A. S. Mischenko, Q. Zhang, R. W. Whatmore, J. F. Scott, N. D. Marthur, *Appl. Phys. Lett.* **2006**, *89*, 242912.

[124] H. Chen, T.-L. Ren, X.-M. Wu, Y. Yang, L.-T. Liu, *Appl. Phys. Lett.* **2009**, *94*, 182902.

[125] US Energy Flow Trends, Lawrence Livermore National Laboratory, https://flowcharts.llnl.gov/#2009, accessed: September 2014.

[126] G. Sebald, D. Guyomar, A. Agbossou, *Smart Mater. Struct.* **2009**, *18*, 125006.

[127] G. Vats, R. Vaish, C. R. Bowen, *J. Appl. Phys.* **2014**, *115*, 013505.

[128] F. Y. Lee, A. Navid, L. Pilon, *Appl. Therm. Eng.* **2012**, *37*, 30.

[129] A. Navid, L. Pilon, *Smart Mater. Struct.* **2011**, *20*, 025012.

[130] R. Kandilian, A. Navid, L. Pilon, *Smart Mater. Struct.* **2011**, *20*, 055020.

[131] F. Y. Lee, S. Goljahi, I. M. McKinley, C. S. Lynch, L. Pilon, *Smart Mater. Struct.* **2012**, *21*, 025021.

[132] R. V. K. Mangalam, J. C. Agar, A. R. Damodaran, J. Karthickm, L. W. Martin, *ACS Appl. Mater. Interfaces* **2013**, *5*, 13235.